PHYSICAL REVIEW B VOLUME 15, NUMBER 2 15 JANUARY 1977

Studies of vibrational surface modes in ionic crystals. I. Detailed shell-model studies for the unrelaxed (001) face of seven crystals having the rocksalt structure*

T. S. Chen and F. W. de Wette
Department of Physics, University of Texas, Austin, Texas 78712

G. P. Alldredge[†]
Department of Physics and Graduate Center for Materials Research, University of Missouri, Rolla, Missouri 65401

(Received 1 March 1976)

We present a comprehensive, unified account of the lattice dynamics of unrelaxed (001) faces of seven crystals having the rocksalt structure, three of which have an absolute gap between the acoustical and optical bulk bands (RbF, RbCl, and NaI) and four of which have overlap between these bulk bands (NaF, NaCl, LiF, and MgO). The results are obtained from calculations of the normal modes of a thin crystal film in which the ionic interactions are described by the rigid-shell model. An outline of the formulation of the shell model for the film is given, and the rapid convergence of surface-phonon frequencies with increasing film thickness is demonstrated. Surface- and pseudosurface-phonon dispersion curves and bulk bands are displayed in the form of the dispersion curves of a 15-layer film over the two-dimensional surface Brillouin zone. The surface-excess phonon density of states $f^s(\omega)$ is given, and its peaks and valleys are correlated with features in the film dispersion curves. The domains of existence and the vibrational character of the more prominent surface-phonon bands are discussed. We establish the relation between the surface modes of the lattice models and the macroscopic surface waves of the dielectric and elastic continuum theories (Fuchs-Kliewer and Rayleigh waves, respectively). Comparison with experiments is made; the agreement with low-energy atom scattering from single-crystal surfaces of LiF and with inelastic neutron scattering from microcrystallite samples of MgO is particularly notable, although the latter comparison also displays some significant discrepancies.

I. INTRODUCTION

In recent years there has been considerable interest in experimental and theoretical studies of surface modes of vibration in ionic crystals. A number of experimental studies have been reported, using various methods such as electron-energy-loss spectroscopy,[1,2] inelastic neutron scattering,[3,4] infrared absorption,[5] and inelastic light-atom scattering.[6,7] In theoretical treatments three different approaches have been used, namely, continuum dielectric theory,[8,9] slab lattice dynamics,[10-20] and the Green's-function method.[21]

In slab lattice-dynamics calculations, two different models have been used, namely, the Kellermann rigid-ion (KRI) model[22] and the more realistic shell model.[23,24] A calculation with the KRI model for a crystal surface was first carried out for NaCl(001) by Lucas[10] at $\vec{q}=0$ ($\vec{q}$ is the two-dimensional wave vector parallel to the surface), and subsequently by Tong and Maradudin[11] for a coarse mesh of values of $\vec{q}$ throughout the two-dimensional surface Brillouin zone (SBZ). The first shell-model calculation for a crystal surface was carried out by Chen *et al.*[16] for NaCl(001). To date, the direct slab lattice-dynamical method has provided the most detailed results on surface vibrations of ionic crystals. In addition, from comparisons of experimental and theoretical results, it is evident that the shell model is superior to the KRI model in obtaining agreement between theory and experiment.

In the present paper we present a summary formulation of the dynamics of ionic crystalline slabs with shell-model interaction, and report results of a comprehensive study of the surface vibrational modes of the unrelaxed (001) faces of seven ionic crystals: six alkali halides (NaF, NaCl, NaI, RbF, RbCl, LiF) and MgO, all having the rocksalt structure. The seven crystals are of two types: one type with a large absolute gap between the optical and acoustic bulk bands, and the other type without such an absolute gap. The calculations for LiF, NaF, and MgO were inspired by the existence of experimental data on these crystals. Although the results reported here are restricted to the unrelaxed case, there are encouraging points of agreement with some experimental results. It is hoped that the present results on seven crystals will be a stimulus for further experimental work on these crystals (e.g., inelastic neutron and light-atom scattering), and the present results will serve as a bench mark for comparison with subsequent studies of the effects of relaxation on the surface dynamics of ionic crystals.

The paper is organized as follows. In Sec. II we outline the formalism. A description of the calculations follows in Sec. III. The general features of vibrational surface modes are described in Sec. IV; some comparisons with experimental results bearing most directly on vibrational surface modes are also included in this section. Related integral properties, such as surface enhancement of the thermal mean-square amplitudes, surface thermodynamic functions, and surface correlation functions are the subject of papers to appear elsewhere.

II. SHELL MODEL AND SLAB DYNAMICS

The shell model was developed to account for long-range Coulomb and short-range overlap polarization effects in ionic crystals. Originally conceived by Dick and Overhauser[23] to describe dielectric effects, the model was subsequently adapted for dynamical calculations, principally by Woods *et al.*,[24] Cochran,[25] and Cowley.[26] This development has been summarized in a number of reviews and need not be repeated here.[27-29]

In this section we summarize the general formulation and notation for the shell-model lattice dynamics of crystal slabs, following notational conventions given by Allen *et al.*[30] The formulation of the shell model that we have used in this work closely resembles that given for infinite crystals in the recent review by Venkataraman *et al.*,[29] to which we refer for details. In order to maintain a unity of approach, we briefly define the slab notation here, state the equations of slab dynamics, and reproduce the salient shell-model equations in Appendix A. We consider crystal slabs with two parallel surfaces, consisting of a finite number of layers perpendicular to the z direction, and extending to infinity in the x and y directions. It is useful to introduce two-dimensional vectors with only x and y components, and to indicate these with superior bars: If $\vec{r}=(x,y,z)$ and $\vec{l}=(l_1,l_2,l_3)$, then $\bar{r}=(x,y)$ and $\bar{l}=(l_1,l_2)$. With this notation the instantaneous position of the κth ionic core in the $\vec{l}$th unit cell can be written as

$$\vec{r}^{\,c}(\vec{l}\kappa)=\vec{r}_0(\vec{l}\kappa)+\vec{u}^{\,c}(\vec{l}\kappa)=\bar{r}_0(\bar{l})+\vec{r}_0(l_3\kappa)+\vec{u}^{\,c}(\vec{l}\kappa) \ , \tag{1}$$

where $\vec{r}_0(\vec{l}\kappa)$ is the mean position of the ion and $\vec{u}^c(\vec{l}\kappa)$ the instantaneous (i.e., time dependent) displacement of the core from its mean position. Similarly, the instantaneous position of the center of the outer shell of the same ion can be written as

$$\vec{r}^{\,s}(\vec{l}\kappa)=\vec{r}_0(\vec{l}\kappa)+\vec{u}^{\,s}(\vec{l}\kappa)=\bar{r}_0(\bar{l})+\vec{r}_0(l_3\kappa)+\vec{u}^{\,s}(\vec{l}\kappa) \ , \tag{2}$$

where $\vec{u}^s(\vec{l}\kappa)$ is the instantaneous displacement of the center of the outer shell from its mean position. The set of numbers $\vec{l}=(l_1,l_2,l_3)$ together with the index κ specify a particular ion; l_3 labels a lattice plane parallel to the surface and (l_1,l_2) specifies a point of the two-dimensional lattice which spans the plane l_3; κ distinguishes the different ions in the unit cell associated with a particular l_3 lattice plane.

Assuming that the total potential energy of the crystal slab $\Phi(\vec{r}^{\,c},\vec{r}^{\,s})$ is a function of the position vectors $\vec{r}^{\,c}(\vec{l}\kappa)$ and $\vec{r}^{\,s}(\vec{l}\kappa)$, we expand $\Phi(\vec{r}^{\,c},\vec{r}^{\,s})$ in a double Taylor series, in which both the core and shell coordinates $\vec{r}^{\,c}(\vec{l}\kappa)$ and $\vec{r}^{\,s}(\vec{l}\kappa)$ are expanded around the mean ionic positions $\vec{r}_0(\vec{l}\kappa)$; we then have

$$\Phi(\vec{r}^{\,c},\vec{r}^{\,s})-\Phi_0=\Phi_1+\Phi_2+\cdots \ . \tag{3}$$

In the quasiharmonic approximation one neglects all terms but the second one on the right-hand side of Eq. (3), the sum of the other terms being considered as a small perturbation. The quadratic term Φ_2 in the double Taylor expansion has the form

$$\begin{aligned}\Phi_2=\frac{1}{2}\sum_{\substack{l\kappa\alpha\\ l'\kappa'\beta}}\big[&\Phi^G_{\alpha\beta}(\vec{l}\kappa;\vec{l}'\kappa')u^c_\alpha(\vec{l}\kappa)u^c_\beta(\vec{l}'\kappa')\\ &+\Phi^F_{\alpha\beta}(\vec{l}\kappa;\vec{l}'\kappa')u^c_\alpha(\vec{l}\kappa)u^s_\beta(\vec{l}'\kappa')\\ &+\Phi^F_{\beta\alpha}(\vec{l}'\kappa';\vec{l}\kappa)u^s_\alpha(\vec{l}\kappa)u^c_\beta(\vec{l}'\kappa')\\ &+\Phi^s_{\alpha\beta}(\vec{l}\kappa;\vec{l}'\kappa')u^s_\alpha(\vec{l}\kappa)u^s_\beta(\vec{l}'\kappa')\big] \ ,\end{aligned} \tag{4}$$

where

$$\Phi^G_{\alpha\beta}(\vec{l}\kappa;\vec{l}'\kappa')=\left(\frac{\partial^2\Phi}{\partial u^c_\alpha(\vec{l}\kappa)\partial u^c_\beta(\vec{l}'\kappa')}\right)_0 \ , \tag{5}$$

$$\Phi^F_{\alpha\beta}(\vec{l}\kappa;\vec{l}'\kappa')=\left(\frac{\partial^2\Phi}{\partial u^c_\alpha(\vec{l}\kappa)\partial u^s_\beta(\vec{l}'\kappa')}\right)_0 \ , \tag{6}$$

$$\Phi^s_{\alpha\beta}(\vec{l}\kappa;\vec{l}'\kappa')=\left(\frac{\partial^2\Phi}{\partial u^s_\alpha(\vec{l}\kappa)\partial u^s_\beta(\vec{l}'\kappa')}\right)_0 \ , \tag{7}$$

where $\alpha,\beta=x,y$, or z, and the derivative quantities are evaluated for all ions and shells at their mean positions. This implies that the quasiharmonic-approximation force constants $\Phi_{\alpha\beta}$ are evaluated for a configuration of the crystal in which bulk thermal expansion and (in principle) surface thermal expansion have been taken into account.

The equations of motion of cores and shells are, respectively,

$$M_\kappa\ddot{u}^c_\alpha(\vec{l}\kappa)=-\frac{\partial\Phi_2}{\partial u^c_\alpha(\vec{l}\kappa)} \ , \tag{8}$$

$$0=\frac{\partial\Phi_2}{\partial u^s_\alpha(\vec{l}\kappa)} \ , \tag{9}$$

where the 0 results from the zero shell mass.

In Appendix A we show that after substantial rearrangement and manipulation of the quantities in these equations, and assuming that the short-range forces are entirely due to shell-shell interactions, the equations of motion can be reexpressed in the form

$$\omega^2 \overleftrightarrow{\xi}^c = \overleftrightarrow{\mathrm{D}} \overleftrightarrow{\xi}^c , \tag{10}$$

with

$$\overleftrightarrow{\mathrm{D}} = (\overleftrightarrow{\mathrm{R}} + \overleftrightarrow{\mathrm{Z}}_d \overleftrightarrow{\mathrm{C}} \overleftrightarrow{\mathrm{Z}}_d) - (\overleftrightarrow{\mathrm{T}} + \overleftrightarrow{\mathrm{Z}}_d \overleftrightarrow{\mathrm{C}} \overleftrightarrow{\mathrm{Y}}_d)(\overleftrightarrow{\mathrm{S}} + \overleftrightarrow{\mathrm{Y}}_d \overleftrightarrow{\mathrm{C}} \overleftrightarrow{\mathrm{Y}}_d)^{-1}(\tilde{\overleftrightarrow{\mathrm{T}}}{}^* + \overleftrightarrow{\mathrm{Y}}_d \overleftrightarrow{\mathrm{C}} \overleftrightarrow{\mathrm{Z}}_d) , \tag{11}$$

where $\overleftrightarrow{\xi}^c$ are the column matrices for the core eigenvectors, $\overleftrightarrow{\mathrm{C}}$ the matrix describing the Coulomb interactions, and $\overleftrightarrow{\mathrm{R}}$, $\overleftrightarrow{\mathrm{T}}$, and $\overleftrightarrow{\mathrm{S}}$ the matrices describing the short-range interactions between neighboring ions, between ions and neighboring shells, and between neighboring shells, respectively. Finally, $\overleftrightarrow{\mathrm{Z}}_d$ and $\overleftrightarrow{\mathrm{Y}}_d$ are the diagonal matrices for the ion and core charges. Equations (10) and (11) constitute the customary way of expressing the equations of motion in the context of the shell model. In Appendix A we briefly sketch the derivation leading from Eqs. (8) and (9) to Eqs. (10) and (11) and in Appendix C we list the expressions for the matrix elements $R_{\alpha\beta}$ and $C_{\alpha\beta}$ as they apply to slab calculations.

III. CALCULATIONS

The calculations described in this paper were carried out for unrelaxed crystal slabs; i.e., we have used the bulk nearest-neighbor distance r_0 as the inter-ion distance throughout the slab and assumed the static dipoles to be zero throughout. In principle, surface relaxation (i.e., the slight displacement of the mean ionic positions and nonzero static dipoles near the surface) can have an important influence on surface dynamic phenomena. However, there are difficulties in developing a shell-model description that is consistent for both static structural properties, such as surface relaxation, and dynamical properties, such as phonon spectra. For example, Benson and Claxton[31] have calculated the static relaxation of the rocksalt (001) surface on the basis of a simple shell model which incorporates static dielectric properties and long-wavelength optical properties; however, their shell model is not adequate to describe accurately the phonons throughout the Brillouin zone (BZ). On the other hand, dynamical shell models, such as we use, do not provide a systematic prescription for modifying the model parameters when the ionic coordinates change from those of bulk equilibrium. For instance, a straightforward extrapolation from the bulk equilibrium configuration for the energy, using a Born-Mayer functional form, does not lead to reasonable results for surface relaxation. (We have incorporated relaxation effects in certain of our preliminary calculations,[32] and will deal with such effects in later publications.) In view of the considerable amount of additional work required to adapt the dynamical shell model for relaxation calculations, we consider it worthwhile to report our shell-model calculations for unrelaxed slabs.

The main objective of slab lattice dynamical calculations is to obtain the vibrational frequencies $\omega_p(\vec{q})$ and the associated vibrational amplitudes $\xi^c_\alpha(l_3\kappa;\vec{q}p)$, by solving the eigenvalue problem, Eq. (10), for a representative set of two-dimensional wave vectors $\vec{q}$. In order to carry out this program, one first has to evaluate the elements of the dynamical matrix, which appears in the right-hand side of Eq. (10). Of these, the elements of the diagonal matrices $\overleftrightarrow{\mathrm{Z}}_d$ and $\overleftrightarrow{\mathrm{Y}}_d$ can be obtained very easily from the parameters of the shell model. However, the derivations of the elements of the (nondiagonal) matrices $\overleftrightarrow{\mathrm{R}}$ and $\overleftrightarrow{\mathrm{C}}$ are both complicated and tedious; this holds, in particular, for the elements of the Coulomb interaction matrix $\overleftrightarrow{\mathrm{C}}$. For this reason we will not present these derivations here, but restrict ourselves to mentioning their salient points, and to providing a list of the matrix elements of $\overleftrightarrow{\mathrm{R}}$ and $\overleftrightarrow{\mathrm{C}}$ in the Appendix C; for details of the derivations we refer to Ref. 15.

Here we make the following specializations to the general formulation for the interactions:

(i) For the short-range interaction, both nearest- and second-nearest-neighbor interactions are taken into account. Most of the existing shell models provide us with six short-range parameters, A^{+-}, B^{+-}, A^{--}, B^{--}, A^{++}, and B^{++}, for the cation-anion, anion-anion, and cation-cation interactions, respectively. The short-range parameters A^{ij} and B^{ij} are defined in the usual fashion:

$$A^{ij} = \left(\frac{2V_a}{e^2}\right) \frac{d^2\Phi^R}{d{r_{ij}}^2}\bigg|_{\mathrm{eq}} , \tag{12}$$

$$B^{ij} = \left(\frac{2V_a}{e^2}\right) \frac{-1}{r_{ij}} \frac{d\Phi^R}{dr_{ij}}\bigg|_{\mathrm{eq}} , \tag{13}$$

where $V_a = 2r_0^3$, r_0 is the nearest neighbor distance, and Φ^R the potential function for the short-range interactions. From Eqs. (12), (13), and (A9) one can derive an expression for $R_{\alpha\beta}(l_3\kappa, l_3'\kappa';\vec{q})$ (remember $\overleftrightarrow{\mathrm{R}} = \overleftrightarrow{\mathrm{S}}$ is assumed) in terms of A^{ij} and B^{ij} (without knowing the explicit form of potential function Φ^R).

(ii) The elements of the Coulomb interaction matrix $\overleftrightarrow{\mathrm{C}}$ contain lattice sums which converge extremely slowly in direct space so that special methods have to be used to improve the convergence. Tong and Maradudin[11] used a modified-Bessel-function transformation to bring the sums into a rapidly convergent form. For the special case of the Coulomb coefficients coupling ions in the same plane, Chen *et al.*[12] obtained a substantial improvement in convergence over the modified-Bessel-function method by using the method of planewise summation,[33] which uses an incomplete-gamma-function transformation. Lucas[10] also used the incomplete-gamma-function transformation but he presented the relevant expressions in a very compact form which is not very transparent. Our expressions in Appendix C are complete and can be used directly.

(iii) The shell models that were used in the present work were taken from several different neutron scattering studies on the corresponding bulk crystals.[34] In addition to the six short-range parameters, the bulk shell model usually gives the electronic and mechanical polarizabilities α_κ and d_κ rather than the shell charge Y_κ and the spring constant K_κ. To obtain the latter we use the relations given by Woods *et al.*,[24] namely,

$$\alpha_\kappa = \frac{Y_\kappa^2}{K_\kappa + [T_{\alpha\alpha}(\kappa)]_0}, \tag{14}$$

$$d_\kappa = \frac{[T_{\alpha\alpha}(\kappa)]_0 Y_\kappa}{K_\kappa + [T_{\alpha\alpha}(\kappa)]_0}, \tag{15}$$

where the subscript 0 indicates the short-range matrix element $T_{\alpha\alpha}(\kappa)$ evaluated at $\vec{q} = 0$.

For a 15-layer slab, there are $2 \times 3 \times 15 = 90$ frequencies for each wave vector $\vec{q}$. In general $\overleftrightarrow{R}$ and $\overleftrightarrow{C}$ are complex Hermitian matrices of dimension 90×90. In the process of constructing $\overleftrightarrow{D}$ we need at least three $2 \times 90 \times 90$ matrices for manipulating the operations in Eq. (11). In order to reduce the computation requirements of storage and time, symmetry is used to the fullest extent. For details about the use of symmetry for slab calculations, we refer to the recent review by de Wette and Alldredge.[35]

After construction of the dynamical matrix $\overleftrightarrow{D}$, the eigenvalue equation can be solved numerically on a high-speed computer (in our case a CDC 6600). Before carrying out the slab calculation, we performed independent bulk calculations with these shell models in order both to assure ourselves that in each case our results for the bulk were indeed identical with those of the original publications and to determine the bulk-band edges for given $\vec{q}$.

The slab calculations for all of the seven crystals (except LiF) have been carried out for a uniform mesh of 66 values of $\vec{q}$ in the irreducible $\frac{1}{8}$th element of the surface Brillouin zone (SBZ) (which is shown in Fig. 1). This gives $66 \times 90 = 5940$ independent sample frequencies, a total of 36 000 frequencies in the whole SBZ. In addition, for the same crystals we performed most of the bulk calculations for a mesh of 422 values of $\vec{q}$ in the irreducible $\frac{1}{48}$th element of the three-dimensional BZ in order to be able to evaluate the surface-excess distribution of frequencies $f^s(\omega)$ (cf. Sec. VI C), the surface enhancement of the thermal mean-square amplitudes,[36] and the other surface-excess thermodynamic quantities (to appear elsewhere). There were $422 \times 6 = 2532$ independent sample frequencies for a total of 82 944 frequencies in the three-dimensional BZ. The results of these calculations will be discussed in Sec. IV.

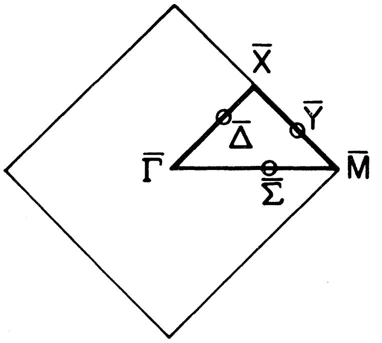

FIG. 1. Two-dimensional surface Brillouin zone (SBZ) for the (001) surface of rocksalt-structured crystals. The high-symmetry directions are $\bar{\Sigma}$ along the [100] direction, $\bar{\Delta}$ along [110], and $\bar{Y}$ running from $\bar{M} = (1, 0, 0)\pi/a$ through $\bar{X} = (\frac{1}{2}, \frac{1}{2}, 0)\pi/a$, where a is the usual cubic lattice constant. An irreducible element of the SBZ is delineated by bold outline.

IV. REVIEW OF RESULTS

Although some of our preliminary results have already been published in earlier communications,[16–18] the present paper presents a comprehensive and unified account of the results for the unrelaxed surface of seven rocksalt-structured crystals. In addition, recent corrections[34(f)] in the bulk shell-model parameters of RbF and RbCl forced us to redo the calculations for these crystals, while extensive new results for NaI and NaF are published here for the first time. Finally, the calculations of the surface-excess frequency distributions $f^s(\omega)$ have been refined by the use of a staggered-bin procedure.[20]

The results of the calculations are presented in plots of the dispersion curves $\omega_p(\vec{q})$, and of the surface-excess frequency distributions $f^s(\omega)$, in separate figures for each of the seven crystals considered (see, e.g., Fig. 2 for RbF). The dispersion curves are given for $\vec{q}$ values along the high-symmetry lines $\bar{\Gamma}\bar{X}$, $\bar{X}\bar{M}$, and $\bar{M}\bar{\Gamma}$. In the figures, the slab dispersion curves lying in the bulk bands are indicated by dashed lines, the surface modes by solid lines, and the (so-called) pseudosurface modes by dash-dot lines. In a few

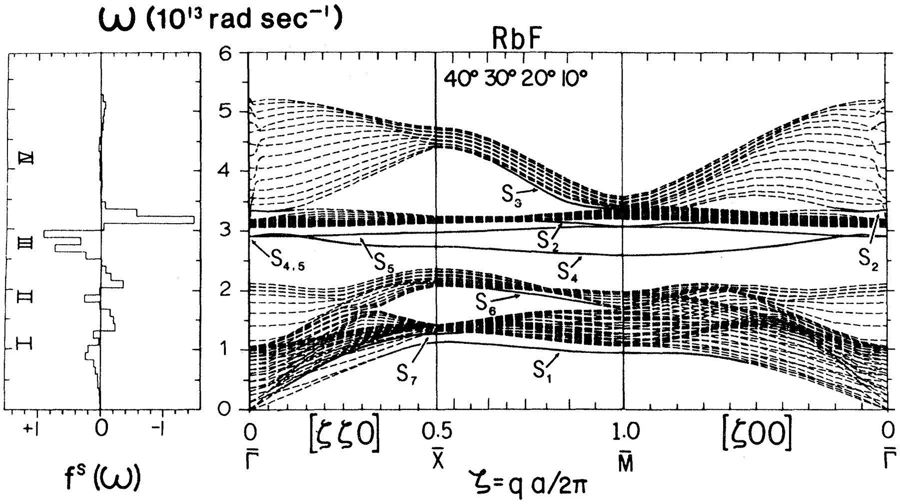

FIG. 2. Dispersion curves and surface-excess distribution of frequencies $f^s(\omega)$ for a 15-layer slab of RbF with free (001) surfaces. Most of the 90 normal-mode branches are bulklike modes within the bulk subbands and are shown as dashed curves; an exception is the Fuchs-Kliewer modes $FK^{\pm}$ which appear as loci of hybridizing modes in the LO bulk subband for $\zeta \lesssim 0.1$. The surface-localized modes lie on branches shown as solid lines are denoted by the labels S_i ($i=1,2,\cdots$) according to an arbitrary scheme. $f^s(\omega)$ is given in units of $(10^{13}\text{ rad sec}^{-1})^{-1}$ per fraction of surface particles. Microscopic surface-mode resonance branches will be denoted by heavy dot-dash curves (none are shown in this figure), and labeled MS_i.

cases (e.g., LiF) we have indicated the boundaries of the bulk bands by dotted lines. The dispersion curves have been computer generated and, except for the traces of the Fuchs-Kliewer modes through the bulklike longitudinal optical (LO) modes near the zone center $\bar{\Gamma}$, crossovers between the various branches have not been resolved.

Because of the presence of two surfaces in the slab, the surface modes occur in quasidegenerate pairs. Each pair of surface modes is indicated by a label S_i ($i=1,2,\ldots,8$) according to an arbitrary scheme, but consistent with our previous conventions of labeling. When the S_i surface-mode branch lies within a bulk band and the surface modes become mixed with bulk modes to form mixed modes, then the resulting pseudosurface branch is labeled MS_i. The corresponding surface-excess frequency distribution $f^s(\omega)$ is shown at the left of the dispersion curves in each of the seven figures. The general features of the results are summarized below.

A. Bulk subbands and gaps

It is well known that for bulk diatomic ionic crystals, there exist six dispersion curves (six degrees of freedom per unit cell), namely, one longitudinal-optical (LO) and two transverse-optical (TO) branches, and one longitudinal-acoustical (LA) and two transverse-acoustical (TA) branches. Thus, a 15-layer slab of the rocksalt structure has 90 dispersion curves. Most of these represent bulk modes and fall into six densely populated *bulk subbands* (corresponding in character to the six bulk dispersion curves). However, a small number of dispersion curves lie either outside the bulk bands, or in gaps between the bulk subbands, and these represent surface modes. In addition there are resonances inside the bulk bands which correspond to modes that have both surface-localized and bulklike components; the terms "mixed mode" and "pseudosurface mode" are also applied to these resonances.

Along the high-symmetry lines $\overline{\Gamma X}$ and $\overline{M\Gamma}$, two-thirds of the 90 modes have polarizations in the sagittal plane; these are the sagittal-plane (SP) modes. One-third are polarized normal to the sagittal plane; these are the shear-horizontal (SH) modes. Of the six bulk subbands, the LO band and one of the TO bands, and the LA band and one of the TA bands consist of SP modes; the remaining TO and TA bands consist of SH modes.

For most of the $\vec{q}$ values along the high-symmetry lines at least some of the bulk subbands overlap each other, while for certain ranges of $\vec{q}$ values there exist gaps between the bulk subbands. The structure of these gaps, which is of great importance for the occurrence of surface modes, usually depends on the kind of crystal that is considered. With respect to the structure of the bulk bands, the seven crystals are of two types. (i) Type A: these crystals exhibit a large absolute gap which completely separates the optical and acoustic bulk bands. This gap is a result of the large disparity of the ion masses in these crystals. Examples are RbF (Fig. 2), RbCl (Fig. 6), and NaI (Fig. 7). (ii) Type B: these crystals do not exhibit the absolute gap of type A, because the mass ratios of the constituent ions are smaller. Examples are NaCl (Fig. 3), NaF (Fig. 8), LiF (Fig. 9), and MgO (Fig. 10).

The results can be summarized as follows:

In type-A crystals there exist three main gaps: (i) an LA-TA gap centered around $\overline{X}$; (ii) an LO-TO gap near the origin $\overline{\Gamma}$, closing up about one third of the distance from $\overline{\Gamma}$ to $\overline{X}$ and opening up wide around $\overline{X}$; and (iii) the absolute TO-LA gap spanning the entire SBZ. Because of the existence of these three large gaps one has an almost complete separation between the optical and the acoustical bulk subbands in RbCl, RbF, and NaI. As a result of this situation, some particular attention, both experimental and theoretical, has recently been paid to the large-gap alkali-halide crystals.

In type-B crystals the structure of the bulk subbands is not nearly as simple. Since the structure of the gaps is much more complicated, owing to the significant overlap of the optical and acoustic bulk subbands, the gaps are much smaller in size and their shapes are much more irregular. Roughly speaking, the LO-TO and LA-TA gaps around $\overline{X}$ and (except for NaCl) the LO-TO gap near the origin $\overline{\Gamma}$ are still present but they differ in size and shape. In Sec. IV B we examine how the domains of existence of surface modes are affected by the gap structure.

B. Surface modes: Macroscopic and microscopic

Vibrational surface modes can be divided into two principal classes: The first class consists of the so-called *macroscopic* surface modes, for which the attenuation distance away from the surface is proportional to the wavelength, and which, therefore, for long wavelengths, extend over considerable distances into the crystal. Since at such wavelengths the atomistic crystal structure (but not its anisotropy) is unimportant, such modes can be found in elastic and dielectric continuum theories. The second class consists of the so-called *microscopic* modes, for which the penetration depth into the crystal is only a few interatomic distances, no matter what the wavelength. There is, in fact, a third class of surface modes which is intermediate to the two principal classes. This class does not exist in the continuum limit of lattice dynamics ("the long-wavelength limit"), but for certain propagation directions it does exist at arbitrarily long wavelength ("long-wavelength regime") and its penetration distance scales not as the wavelength, but as the square of the wavelength.[37]

In principle microscopic surface modes and macroscopic surface modes (at large wave vectors) can be identified by examining the squares of the polarization vectors of both the anion and the cation, i.e.,

$$
\begin{aligned}
|\vec{\xi}(m,\kappa)|^2 &= |\xi_x(m,\kappa)|^2 + |\xi_y(m,\kappa)|^2 + |\xi_z(m,\kappa)|^2 \\
&= M_\kappa |\vec{u}(m,\kappa)|^2, \qquad (16)
\end{aligned}
$$

as a function of layer index m (increasing away from the surface); these are the so-called attenuation curves. When a dispersion curve is found outside a bulk subband or inside a gap, such a curve can be identified immediately as belonging to a surface mode, without recourse to an attenuation curve being necessary. On the other hand, if a surface mode is surrounded by bulk modes of its own symmetry type of polarization, one must examine the attenuation curve for identification of its surface-localized character; in the first case the surface mode has interaction with the surrounding bulk modes and is in effect a mixed or pseudosurface mode (e.g., MS_4 in Fig. 3). In the case that a surface mode is surrounded by bulk modes of a different symmetry type no interaction with the surrounding bulk modes can occur because the surface mode is decoupled from the surrounding bulk modes; hence it exists as a pure surface mode (e.g., S_5 and S_7 in Fig. 3).

The simplest kind of attenuation curve of a surface mode is that exhibiting an exponential decay with distance from the surface. Although the surface modes S_5 exhibit this kind of behavior, for most surface modes the attenuation curves are considerably more complex. As examples, in Fig. 4, we present for NaCl the attentuation curves for S_4 and S_5 calculated for the wave vector at $\overline{X}$; since the Na^+ and Cl^- ions have different vibrational patterns in these modes (as, of course, they do in all modes) there are four attenuation curves. Notice that the maximum amplitude of both surface modes is in the outer layer for the Na^+ ions but in the second layer for the Cl^- ions. (In fact, in S_5 at $\overline{X}$ the Na^+ ion has zero amplitude for $m = 2, 4, 6, \ldots$, where the Cl^- ion has zero amplitude for $m = 1, 3, 5, \ldots$.)

In the present investigation of the surface vibrations of the (001) face of rocksalt-structured slabs, we have found eight pairs of surface modes to exist in crystals of type A, and eight or fewer pairs of surface modes to exist in crystals of type

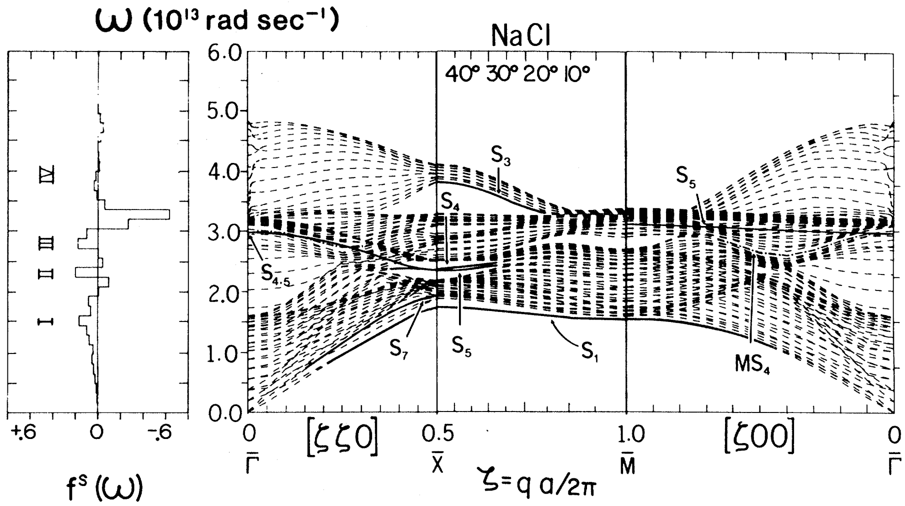

FIG. 3. Dispersion curves and surface-excess distribution of frequencies $f^s(\omega)$ for a 15-layer slab of NaCl with free (001) surfaces. (For notational conventions, see caption of Fig. 2.)

B. Two of these pairs are macroscopic surface modes, namely, the Rayleigh modes S_1 and the Fuchs-Kliewer modes; the other six pairs are either microscopic modes or modes of the intermediate third class. We briefly discuss the character and appearance of these modes.

(a) S_1: By our labeling convention, S_1 is the branch of surface-mode pairs lowest in frequency for each $\vec{q}$ in the SBZ. It is peeled down from the bottom edge of the TA bulk bands by the perturbation imposed on the dynamics of the bulk crystal by the free-surface boundary condition. Along $\overline{\Gamma M}$ and at long wavelength, S_1 is the Rayleigh surface wave which was first described by Lord Rayleigh for isotropic elastic media and which has been generalized subsequently for anisotropic media.[38] S_1 is also the Rayleigh wave along $\overline{\Gamma X}$ for those crystals having a cubic anisotropy parameter $\eta\ [=2c_{44}/(c_{11}-c_{12})]<1$, a class that includes five of the seven crystals in the present study. For those crystals having $\eta>1$, LiF and MgO, S_1 along $\overline{\Gamma X}$ is the SH surface mode of the intermediate third class[37]; between the $\overline{\Gamma X}$ and $\overline{\Gamma M}$ directions S_1 undergoes a smooth transition between the two different mode characters as S_1 transfers its SH character to S_7 (discussed below) and S_7 transfers its SP character to S_1, with the transition most pronounced in the neighborhood of 30° off $\overline{\Gamma M}$, as can be seen in the dispersion curves along $\overline{XM}$.

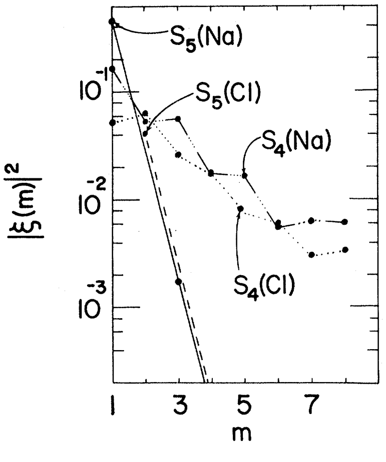

FIG. 4. $|\xi(m,\kappa)|^2$ versus layer index m for S_4 and S_5 of NaCl at the point $\bar{X}$. The eigenvectors are normalized such that $\sum_{m,\kappa}|\vec{\xi}(m,\kappa)|^2=1$, and the curve is the arithmetic mean of the even and odd members of the indicated mode pair. Note that symmetry at $\bar{X}$ forces anion components of S_5 to vanish at the surface ($m=1$) and at all other odd-numbered layers, while cation components of S_5 vanish in the first subsurface ($m=2$) and all other even-numbered layers.

(b) *FK*: The Fuchs-Kliewer modes (labeled by *FK*) are optical surface modes, first obtained by Fuchs and Kliewer[8] in studies of ionic slabs based essentially on dielectric continuum theory; they are SP modes. In our shell-model calculations, the *FK* modes consist of two branches of pseudosurface modes (except for part of the branch FK^- in the LO-TO gap around the origin $\bar{\Gamma}$) represented by a locus of hybridizing branches in the LO and TO bulk subbands near the origin. FK^- (corresponding to Fuchs and Kliewer's ω_-), the lower branch, is of *even* symmetry with respect to reflection in the median plane of the slab, and it starts at $\bar{\Gamma}$ at the bottom of the TO band, moves up through this band and the LO-TO gap and into the LO band (details of these hybridizations for very small wave vectors are given in Fig. 5). The upper branch (*odd* symmetry), FK^+, starts at $\bar{\Gamma}$ at the top of the LO band, moves down inside this band, and joins up with FK^- somewhere in the

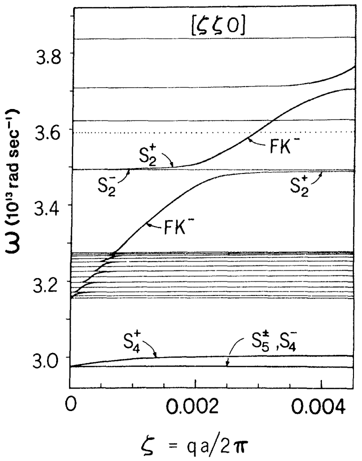

FIG. 5. Detailed dispersion curves for FK^-, $S_2^\pm$, S_4^+, and $S_5^\pm$ of RbF in the vicinity of $\overline{\Gamma}$, for a very fine mesh of two-dimensional wave vectors (one-hundredth of the coarse mesh of Fig. 2). Bulklike branches are shown as fine solid lines. Surface modes and surface-localized segments of hybridizing modes (FK^-) are shown as heavier solid lines. The lower edge of the bulk LO subband is delineated as a dotted line, since the lowest LO bulklike mode in the 15-layer slab is noticeably higher than the band edge. S_i^+ and S_i^- are, respectively, the even and odd members of the ith pair of surface modes; FK^- is the lower FK branch and it is *even*. Note that the SH and SP bulklike modes of the TO subband are degenerate within the resolution presented in the figure.

upper half of the LO band. For larger wave vectors the FK modes merge with the bulk bands; i.e., they lose their surface-localized character.

To the question of what is the limiting frequency of FK^- as $\vec{q} \to 0$, there have been two seemingly different answers: Jones, Fuchs, and Kliewer[13,39] assert that the limiting frequency is that of the SP Lucas modes (which we call S_4 below), whereas in previous papers[14-18] we state that the bulk TO frequency ω_{TO} is the limiting frequency of FK^-, as it is in dielectric continuum theory. There is actually no difference between the two groups based on the primary results of calculation; the difference is one arising from different choices of the criterion for interpreting what the limit is to be. We may illustrate the point by reference to Fig. 5, which gives our dispersion curves for the RbF(001) slab for frequencies in the neighborhood of ω_{TO} on the very fine mesh of $\vec{q}$ near $\overline{\Gamma}$. Jones *et al.* choose as their criterion for the limit of FK^- what we may call the nodal character of FK^-. In dielectric continuum theory, FK^- is a mode symmetric in the coordinate z and it has no nodes between the surface and the median plane. In lattice dynamics, the discreteness of the field makes the concept of nodes somewhat imprecise, but there are occurrences of relatively small values of $|\vec{\xi}(l_3)|^2$ at some l_3, which can be thought of as being near nodes. Thus, because S_4^+ is "nodeless" in this sense at $\overline{\Gamma}$, but immediately developes a "node" as $\vec{q}$ leaves $\overline{\Gamma}$, and because the branch labeled FK^- in Fig. 5 appears to be nodeless where it is sufficiently far from a hybridization with an even bulk branch or the even members of S_2, Jones *et al.* identify S_4^+ at $\overline{\Gamma}$ as the limit of FK^-. On the other had, if one chooses as the criterion the locus of the FK^- dispersion curve as we have done, it is clear from Fig. 5 that the FK^- dispersion curve does not literally connect to S_4^+ as $\vec{q} \to 0$, but instead connects to the lowest even TO bulk mode which converges to ω_{TO} as the slab thickness increases. That is, in the TO bulk band and in the LO-TO gap, FK^- can be readily traced as a continuous dispersion curve as $\vec{q} \to 0$, except where it encounters S_2^+ or an even-parity bulk mode in a region of hybridization, and the lowest TO bulk branch is the terminus of the last segment of FK^- in the TO bulk band. There is *no* continuous dispersion curve in the interval between the S_4,S_5 complex and the bottom of the TO bulk band, an interval which in RbF is greater than the width of the TO bulk band and over half the width of the LO-TO gap. This connectivity of the FK^- trace is what leads us to our statement of its limit. There is, to be sure, some apparent interaction between FK^- and S_4^+: In addition to the exchange of nodeless character mentioned already, S_4^+ is split upward in frequency about 1% (for 15 layers) of its $\overline{\Gamma}$ value as $\vec{q}$ leaves $\overline{\Gamma}$; this splitting is inversely related to the thickness of the slab. So in the absence of a more fundamental principle, the question of the limit of FK^- may be inherently ambiguous.

(c) S_4 *and* S_5: These two microscopic surface modes are transverse-optical surface modes (TOSM) at the long-wavelength limit, originally found by Lucas[10] at $\vec{q} = 0$ in his KRI model calculation for a NaCl slab. The existence of S_4 and S_5 at $\vec{q} = 0$ and for finite wave vectors has been confirmed by Tong and Maradudin,[11] Chen *et al.*,[12] and Jones and Fuchs[13] in independent calculations with the same KRI model. One of the important features is that S_4 and S_5 are degenerate at the origin $\overline{\Gamma}$. The polarization of S_4 is SP and that of S_5 is SH. (i) For type-A crystals S_4 and S_5 are the dominating surface modes in the gap. Since they are well separated from the bulk bands, they both exist for rather large regions of the SBZ, except that in RbCl S_4 rises into the TO bulk band not far from $\overline{\Gamma}$. The clear definition of S_4 and S_5 in these crystals is favorable for a direct experimental verification of their existence. However, no *direct* experimental verification has been made

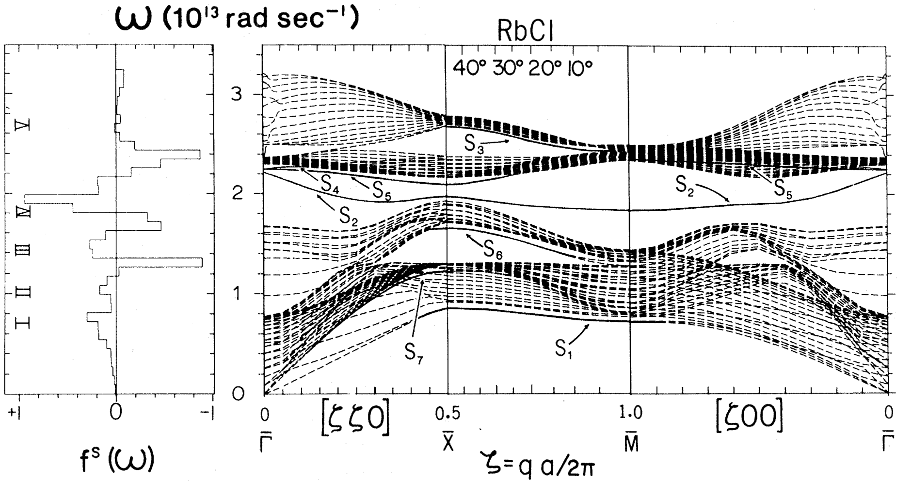

FIG. 6. Dispersion curves and surface-excess distribution of frequencies $f^s(\omega)$ for a 15-layer slab of RbCl with free (001) surfaces. (For notational conventions, see caption of Fig. 2.)

so far for *any* of the microscopic surface modes in type-A crystals. (For *indirect* experimental evidence see Sec. IV E). (ii) For type-B crystals, as $\vec{q}$ is increased from zero, along the $\bar{\Gamma}\bar{X}$ and $\bar{\Gamma}\bar{M}$ directions the modes S_4 mix with the surrounding LA bulk modes and become pseudosurface modes MS_4 immediately. In the gap near $\bar{X}$, MS_4 reappears as a surface mode, as is shown by its attenuation curves for NaCl in Fig. 4. As mentioned above, S_5 is rigorously decoupled from the surrounding bulk modes, so S_5 persists as a surface mode in both the $\bar{\Gamma}\bar{X}$ and $\bar{M}\bar{\Gamma}$ directions, except that in NaF, LiF, and MgO S_5 encounters the SH TO bulk band on the way from $\bar{\Gamma}$ to $\bar{M}$ and then becomes a pseudosurface mode.

(d) S_2: Another important pair of microscopic surface modes, found first in RbF and RbCl by Chen *et al.*,[17] are the longitudinal-optical surface modes (LOSM) S_2. In some cases, S_2 exists both at $\bar{\Gamma}$ and at finite wave vectors; the polarization of S_2 is SP type and at long wavelength the particle motion is predominantly vertical. (i) For type-A crystals, the appearance of S_2 is much less predictable than that of S_4 and S_5. For instance, in RbF, S_2 appears only in the absolute gap around $\bar{M}$ and in the small LO-TO gap around the origin $\bar{\Gamma}$; in both cases it lies higher than S_4 and S_5. However, in RbCl, S_2 is peeled down from the LO bulk subband far below S_4 and S_5 and becomes the dominant surface mode in the absolute gap. Finally, in NaI, S_2 is inside the TO bulk subband at the origin $\bar{\Gamma}$ and becomes a mixed mode for small $\vec{q}$. It reappears around $\bar{M}$ as a surface mode in the absolute gap. (ii) For type-B crystals, S_2 only exists in the small LO-TO gap around the origin in NaF. It is absent in all three other crystals, although it may exist as a weak resonance in a bulk band.

S_2, S_4, and S_5 are the only microscopic surface modes existing for $\vec{q}=0$. At this point S_4 and S_5 are rigorously degenerate and their polarization vectors are parallel to the surface; S_2 is linearly polarized in the z direction (normal to the surface). For increasing $\vec{q}$ along the high-symmetry lines $\bar{\Gamma}\bar{X}$ and $\bar{\Gamma}\bar{M}$, the polarizations of S_4 and S_2 (both SP-type modes) become elliptical parallel to the sagittal plane while S_5 remains SH polarized. In RbF and NaI, a hybridization between S_4 and S_2 occurs along $\bar{\Gamma}\bar{X}$ and $\bar{\Gamma}\bar{M}$ at about one-tenth of the way out from $\bar{\Gamma}$. As a result, at $\bar{M}$ S_4 is polarized in the z direction and S_2 is linearly polarized parallel to $\bar{\Gamma}\bar{M}$.

(e) S_3: S_3 is a microscopic surface mode which exists in the LO-TO gap near the zone boundary $\bar{X}\bar{M}$. It is an optical surface mode peeled down from the LO bulk subband into the LO-TO gap. This mode was first discovered in our NaCl calculation with the KRI mode.[12] In the present work we find the behavior of S_3 to be very similar for all seven crystals. Because of its proximity to the LO bulk subband and its limited appearance at large wave vectors only, it will probably be very difficult to obtain direct experimental verification of the existence of S_3.

(f) S_7: According to our labeling conventions, S_7 is the branch of TA surface-mode pairs lying above S_1 in the long-wavelength regime along $\bar{\Gamma}\bar{X}$. It appears for all seven crystals. Just as the vibrational character of S_1 depends on the cubic anisotropy, so does that of S_7. For $\eta<1$ (i.e., except for LiF and MgO), S_7 is an SH surface mode, since for this anisotropy the SH TA bulk-band edge lies higher than that of the SP TA bulk-band edge. For $\eta>1$, S_7 is an SP surface mode embedded in a background of SH TA bulk modes. As $\vec{q}$ swings away from the $\bar{\Gamma}\bar{X}$ direction, S_7 couples with the background TA bulk modes, where it is embedded and becomes a pseudosurface

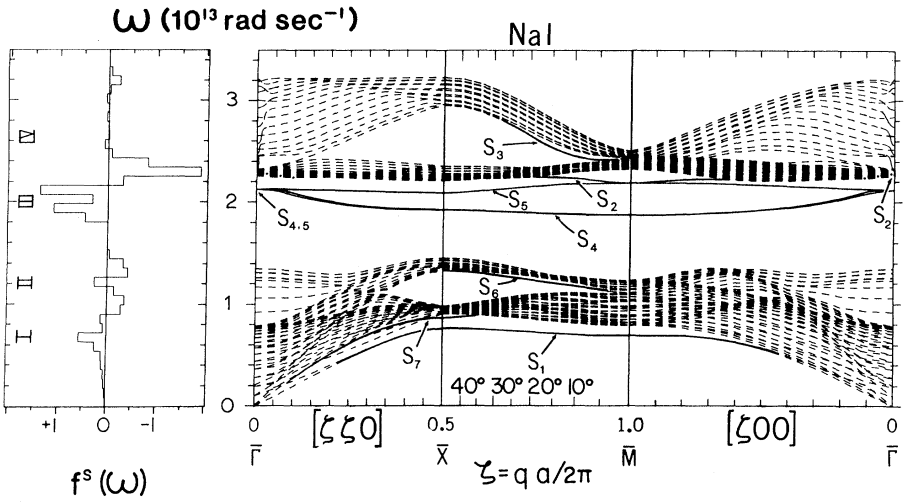

FIG. 7. Dispersion curves and surface-excess distribution of frequencies $f^s(\omega)$ for a 15-layer slab of NaI with free (001) surfaces. (For notational conventions, see caption of Fig. 2.)

mode; for RbF, NaI, NaF, and LiF, S_7 clears the background TA bulk band before it reaches $\bar{X}$ and consequently exists as a pure surface branch away from $\bar{\Gamma}\bar{X}$ in a neighborhood of $\bar{X}$. For $\eta > 1$, S_7 and S_1 undergo a hybridization as $\vec{q}$ swings away from $\bar{\Gamma}\bar{X}$, with the interaction being most pronounced about 25° to 30° off $\bar{\Gamma}\bar{M}$; in the long-wavelength limit for this anisotropy, S_7 is the pseudo-Rayleigh wave described by Lim *et al.*[40] for Cu(001).

(g) S_6: S_6 is a microscopic acoustic surface mode peeled down from the LA subband. For type-A crystals it appears in the LA-TA gap along the zone boundary $\bar{X}\bar{M}$. But for type-B crystals the appearance of S_6 becomes unpredictable because of the strong overlap of the acoustic and optical bulk bands.

We conclude this subsection by listing in Table I the frequencies of all important surface modes at the high-symmetry points for all seven crystals.

C. Surface-excess distribution of frequencies $f^s(\omega)$

The surface-excess distribution of frequencies $f^s(\omega)$ is defined as

$$f^s(\omega) = (N/n)[f^{\text{slab}}(\omega) - f^{\text{bulk}}(\omega)], \tag{17}$$

where N is the total number of ions in the slab, and n the number of surface ions; for a 15-layer slab $N/n = 7.5$. Here, $f(\omega)$ is the frequency distribution function for the slab or the bulk, defined such that $f(\omega)\,d\omega$ is the fraction of the vibrational frequencies in the interval between ω and $\omega + d\omega$. The normalization relation for $f^{\text{slab}}(\omega)$ or $f^{\text{bulk}}(\omega)$ is

TABLE I. Summary of surface-mode frequencies (in units of 10^{13} rad sec^{-1}) at high-symmetry points in the SBZ.

Mode		RbF	RbCl	NaI	NaCl	NaF	LiF	MgO
$\bar{\Gamma}$	S_2	3.345	2.215	2.274	···	5.184	···	···
	$S_{4,5}$	2.905	2.248	2.117	2.980	4.447	5.291	6.774
$\bar{X}$	S_2	···	1.970	···	···	···	···	···
	S_3	4.405	2.680	···	3.818	···	10.235	10.980
	S_4	2.725	···	1.917	2.362	3.558	5.467	6.256
	S_5	2.965	2.090	2.804	2.346	3.534	4.720	5.682
	S_6	···	1.654	1.322	···	2.979	···	4.901
	S_7	1.263	1.227	8.595	1.933	2.985	3.676	5.201
	S_1	1.115	0.857	7.585	1.735	2.874	2.986	4.323
$\bar{M}$	S_2	3.068	1.836	2.182	···	···	···	···
	S_4	2.591	2.343	1.868	···	···	5.804	···
	S_5	3.068	2.343	2.182	3.105	···	···	···
	S_6	···	···	···	···	2.642	···	···
	S_1	0.946	0.724	0.687	1.530	2.556	3.803	5.050

$$\int d\omega f(\omega) = \sum_i \Delta\omega f(\omega) = 1, \qquad (18)$$

where $\Delta\omega$ is the channel width of the histogram form of $f(\omega)$. All $f^s(\omega)$ histograms reported in this paper were obtained by a ninefold staggered-bin smoothing procedure. That is, the smoothed number of frequences in a given channel $(\omega, \omega + \Delta\omega)$ is the average number of frequencies in the nine channels shifted from the reference channel by $j\Delta\omega/9$ $(j = 0, \pm1, \pm2, \pm3, \pm4)$, with each shifted channel assigned the weight $\frac{1}{9}$. From Eqs. (17) and (18) it is evident that $f^s(\omega)$ integrates to zero. In general, $f^s(\omega)$ will exhibit a succession of peaks and valleys, indicating that the occurrence of surface modes is accompanied by the depletion of an equal number of bulk modes. Some caution is urged in the inference of details of surface-mode existence from the surface-excess distribution of frequencies. In some frequency intervals, a positive contribution due to the presence of surface branches in some part of the SBZ can be largely canceled by the depletion of bulk bands required in other regions of the SBZ; a notable example is provided by S_2 in RbF, NaI, and NaF. Although S_2 is fairly flat and occurs over a considerable part of the SBZ, its contributions to $f^s(\omega)$ are swamped by the depletion of the flat TO bulk band which accompanies the formation of S_4 and S_5.

The results for $f^s(\omega)$ are shown on the left of each of the seven dispersion curves. The scale used to display the $f^s(\omega)$ histogram is determined by Eqs. (17) and (18). Note that the magnitudes of the peaks and valleys near ω_{TO} are larger for type-A than for type-B crystals; on the other hand, the magnitude of the lowest peak, peak I, is approximately the same for both types.

We summarize the results as follows:

(a) RbF, Fig. 2: the positive peaks can be identified as I, a resolved doublet due to S_1 and S_7; II, due to S_6; III, a resolved doublet due to S_4 and S_5; and IV, due to S_2 and the lower reaches of S_3 and the *FK* modes.

(b) RbCl, Fig. 6: the peaks can be identified as I, due to S_1; II, due to S_7; III, due to S_6; IV, due mainly to S_2 and partially to S_5; V, due to the lower reaches of S_3 and the *FK* modes.

(c) NaI, Fig. 7: the peaks can be identified as I, a resolved doublet due to S_1 and S_7; II, due to S_6; III, a resolved doublet due to S_4 and S_5; IV, due to the lower reaches of S_3 and the *FK* modes.

(d) NaCl, Fig. 3: the peaks can be identified as I, due to S_1 and S_7; II due to S_4 and S_5 in the gap around $\bar{X}$; III, due to S_5, the resonance MS_4, and resonances associated with the small gaps at $\bar{X}$ and $\bar{M}$ near 3×10^{13} rad/sec (the latter are unlabeled here, but were labeled MS_6 and MS_8 in Ref. 16); IV, due to S_3 and the *FK* modes.

(e) NaF, Fig. 8: the peaks can be identified as I, due to S_1, S_6, and S_7; II, due to S_4 and S_5 in the gap around $\bar{X}$; III, due to S_5, MS_4, and quite likely some unidentified resonance near the SBZ boundary; IV, an apparent weak triplet due to S_2, S_3, and the *FK* modes.

(f) LiF, Fig. 9: the peaks can be identified as I, due to S_1 and S_7; II, due to S_4 and S_5; III, due to S_3 and the *FK* modes. Note that $f^s(\omega)$ for LiF has the highest precision of this series of calculations; it was derived from a sample of 231 points in the irreducible element of the SBZ.

(g) MgO, Fig. 10: the peaks can be identified as I, due to S_1, S_6, and S_7; II, due to S_4 and S_5; III, due to the lower reaches of S_3 and possibly some unidentified resonances; IV, due to the upper reaches of S_3 and the *FK* modes.

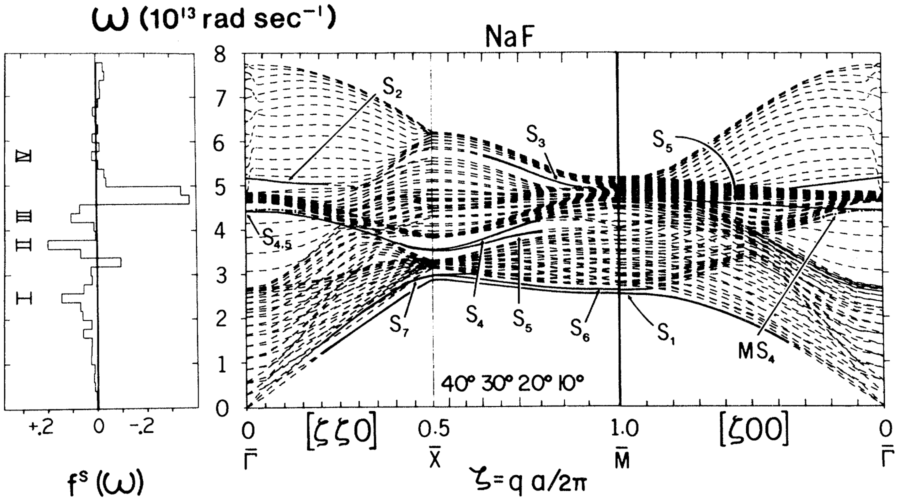

FIG. 8. Dispersion curves and surface-excess distribution of frequencies $f^s(\omega)$ for a 15-layer slab of NaF with free (001) surfaces. (For notational conventions, see caption to Fig. 2.)

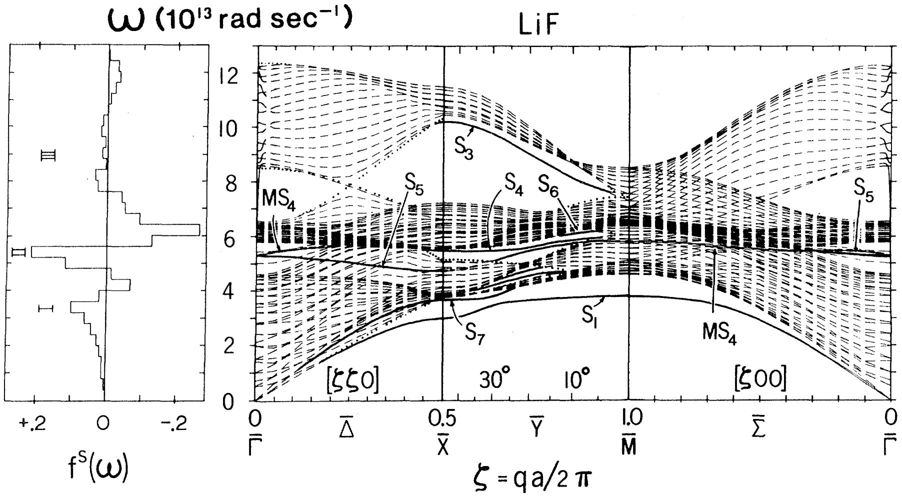

FIG. 9. Dispersion curves and surface-excess distribution of frequencies $f^s(\omega)$ for a 15-layer slab of LiF with free (001) surfaces. (For notational conventions, see caption to Fig. 2). The slab mesh used for the dispersion curves was twice as dense as that used in the other figures (231 points versus the usual 66 points in the irreducible element of the SBZ). The bulk mesh used for the calculation of $f^s(\omega)$ was also denser than in the other cases (913 points versus the usual 422 points in the irreducible element of the bulk BZ). Along $\bar{\Delta}$ and $\bar{Y}$, dotted lines delineate some bulk-band edges.

D. Effects of slab thickness

In this subsection we discuss the effect of slab thickness on the calculated macroscopic and microscopic surface modes. We already pointed out in Sec. IV B that the penetration of the macroscopic surface modes is much deeper into the slab-shaped crystal than that of the microscopic surface modes. One therefore expects the macroscopic surface modes to be much more dependent on the slab thickness than the microscopic modes. On the other hand, there exist many more microscropic than macroscopic surface modes. In order to have assurance about the validity of our results we investigated how these results depend on slab thickness and which slab thicknesses are sufficient for acceptably accurate results. Some of the results of calculations for different slab thicknesses are summarized in Table II.

One criterion that can be applied is the degeneracy of S_4 and S_5, which should occur at the origin $\bar{\Gamma}$ [see Table II(a)]. In our earlier KRI model calculation, we found that the degeneracy of S_4 and S_5 (to the sixth significant figure) can be achieved in a 15-layer calculation; on the other hand, in a shell-model calculation we obtain this degeneracy (to the same accuracy) already in a nine-layer calculation. This is another demonstration of the superiority of the shell model *vis-à-vis* the KRI model.

In Table II(b) we show the thickness effect on the pure microscopic surface modes S_5 and the macroscopic Rayleigh modes. We find that for a 15-

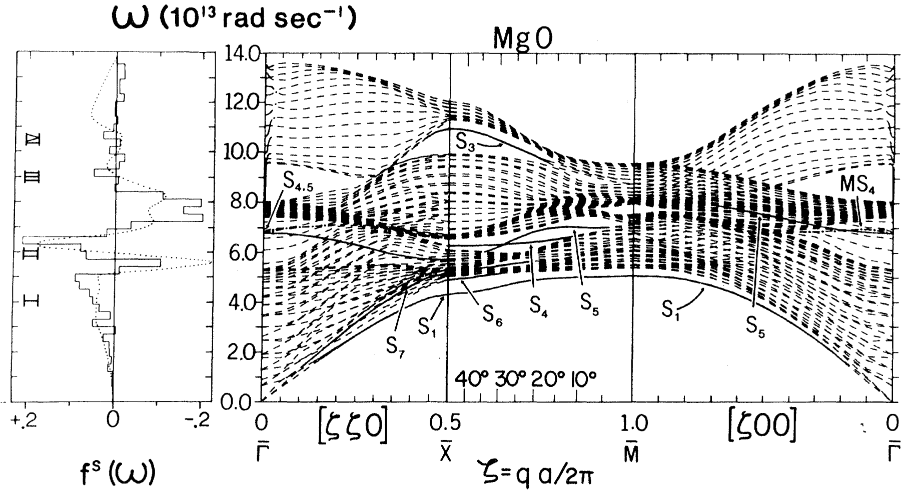

FIG. 10. Dispersion curves and surface-excess distribution of frequencies $f^s(\omega)$ for a 15-layer slab of MgO with free (001) surfaces. (For notational conventions, see caption to Fig. 2.) The surface-excess distribution of frequencies of Rieder and Hörl [Refs. 3(b)] is shown by a dotted line in the left-hand panel; it is scaled in *arbitrary* units so as to fit into the $f^s(\omega)$ frame.

TABLE II. Illustration of the convergence of surface-mode frequencies (in units of 10^{13} rad sec^{-1}) with increasing slab thickness. KRI denotes the Kellermann rigid-ion-model result, and SM denotes the shell-model result.

(a)

Modes \ No. of layers	NaCl (KRI), $\bar{\Gamma}$			NaCl (SM), $\bar{\Gamma}$	
	7	11	15	9	15
S_4	2.418 76	2.418 43	2.418 42	2.979 902	2.979 902
S_5	2.418 09	2.418 41	2.418 42	2.979 902	2.979 902

(b)

Modes \ No. of layers	NaCl (SM), $\bar{X}$		LiF (SM), $\zeta = (0.2, 0)$	
	9	15	15	21
S_5	2.345 657	2.345 655	5.382 035	5.382 035
	2.345 653	2.345 655	5.382 035	5.382 035
Rayleigh	1.735 811	1.735 685	1.330 395	1.312 279
	1.734 850	1.734 972	1.295 611	1.309 037

layer slab the degeneracy of the frequencies of the pair S_5 at $\bar{X}$ is achieved to the seventh significant figure. On the other hand, for the Rayleigh modes we find that the splitting of the frequencies in the pair is larger than that of S_5 and does not diminish as fast with increasing slab thickness.

On the basis of these comparisons we can conclude that the accuracy of the 15-layer slab results is excellent for the microscopic surface modes, and quite acceptable for the Rayleigh modes over most of the SBZ.

E. Comparison with experimental results

Although the investigation of vibrational surface modes has gained increasing interest in recent years, the more common experimental methods probe only the long-wavelength region around the origin $\bar{\Gamma}$. Two most notable exceptions are the inelastic light-atom and neutron scattering experiments.

For those experiments which probe only the long-wavelength region, we can only give an indirect comparison with our results. The early work of Boersch *et al.*[1] on electron-energy-loss spectroscopy can be used as an example. These authors reported observations of energy-loss spectra with maxima in a range from 0.042 to 0.050 eV in LiF foils, and they attributed these peaks to interactions with the FK^- mode. We found that the energy range of the peaks matches the LO-TO gap around the origin, which lies between $\omega \simeq 6.5 \times 10^{13}$ rad/sec (0.043 eV) and $\omega \simeq 8.5 \times 10^{13}$ rad/sec(0.056 eV) in our calculation for the LiF slab. This finding may suggest that the FK^- branch is more easily detected in a gap.

Now we turn to the more direct comparisons with the inelastic light-atom and neutron scattering experiments. In the inelastic atomic scattering, results are available from two groups of experimentalists. We first mention the results of Williams[6(a)] on LiF(001)-He scattering and of Mason and Williams[6(b)] on NaF(001)-He scattering. In the first case, from his analysis of the experimental data, Williams determined a dispersion curve for Rayleigh waves along [100] for the (001) face which agrees fairly well with the results predicted by continuum theory. The ratio of the Rayleigh wave phase velocity to the transverse bulk phase velocity obtained by Williams is 0.81; the result for this ratio from our shell-model calculation is 0.813. Thus the agreement between the LiF-He scattering experiment and the two theoretical results is very good. For the NaF-He scattering, a similar analysis by Mason and Williams yielded points which are taken to represent the dispersion curve of the Rayleigh waves; however, these results showed much greater scatter and the mean curve through them falls considerably below the theoretical line at long wavelengths. In comparison, the ratio of Rayleigh wave velocity to transverse bulk wave velocity is 0.95 from continuum theory and 0.932 from our shell model.

A second LiF(001)-Ne scattering experiment was performed by Boato and co-workers at the University of Genoa (cited in Ref. 7). After his analysis of the experimental data, Benedek[7] reported experimentally fitted frequencies for the Rayleigh modes at $\bar{M}(R_M)$, and the Lucas modes at $\bar{\Gamma}(L_\Gamma)$, $\bar{M}(L_M)$. Here we list the frequencies of these modes (in units of 10^{13} rad/sec) from experimental analysis, Benedek's Green's-function (GF) method, and our shell-model (SM) slab calculation[41]:

$R_M = 3.91$(expt), 3.95(GF), 3.80(SM slab),
$L_\Gamma = 5.42$(expt), 5.84(GF), 5.29(SM slab),
$L_M = 5.95$(expt), 6.15(GF), 5.80(SM slab),

The overall agreement is quite good. However, notice that all the frequencies in the shell model are smaller than the measured ones. This might indicate that a small inward surface relaxation, which would raise the surface-mode frequencies, has been neglected in our shell-model slab calculation.[42]

Finally, we turn to a discussion of the results of inelastic neutron scattering from samples of microcrystallites, from which an experimental curve can be obtained for $f^s(\omega)$, the surface-induced change in the phonon density of states. As we discussed in Sec. IV C, the major features in $f^s(\omega)$ can often be correlated rather clearly with specific portions of the surface-phonon bands and their associated bulk-band depletions. To date, microcrystallite samples of two rocksalt-structured crystals, magnesium oxide[3] and titanium nitride,[4] have been studied with inelastic neutron scattering.

Titanium nitride belongs to the type-A crystal defined in Sec. IV A. Conduction electrons play a substantial role in the bulk lattice dynamics of the transition-metal carbides and nitrides,[43] so that the simple shell model used in the present study cannot be adequate for TiN. Nevertheless, there is a qualitative resemblance between Rieder and Drexel's surface-excess density of states for TiN and our $f^s(\omega)$ for type-A crystals, especially RbF and NaI. For TiN, there is a peak I, a depletion valley in the TA-LA bulk band just above peak I which has the hint of a peak II in it, a resolved doublet peak III between the LA and TO bulk bands, and a peak IV near the upper limit of the bulk density of states. The lower subpeak III overlaps the upper extent of the bulk LA subband enough that Rieder and Drexel speculate that it may be due primarily to a band of LA surface modes pushed up from the LA bulk band. The minimum value in the valley between the two subpeaks of peak III is, however, sufficiently large to permit a hypothesis that the lower subpeak III is due to a TO surface band such as S_4 near a (surface) critical point, with the high values in the valley due to this surface band crossing that spectral region farther away from a surface critical point. At the present stage of development, we cannot choose between these two hypotheses on the type of surface modes contributing to the lower subpeak III; accounting for the role of conduction electrons in both surface statics and dynamics of materials such as TiN is a problem even more difficult than the still unsolved problem of surface relaxation in the closed-shell ionic systems which are the subject of the present paper.

We are able to make a direct comparison with the inelastic-neutron-scattering results for MgO, a crystal of type B. The refined result[3(b)] of Rieder and Hörl's[3(a)] measurement on MgO is shown as the dotted curve on the left side of Fig. 10 [this curve is based on more extensive neutron scattering data than the original curve of Ref. 3 (a)]. Because of difficulties in the experimental-determination of the specific surface area of a powder sample we have not attempted to standardize the two curves to the same $f^s(\omega)$ scale in Fig. 10 (the scale for the experimental curve is arbitrary). Instead we concentrate on the location of features in the curve and their relative magnitudes. There is good agreement in the locations of peaks I and II and the valley between them. The valley just above II also appears to be in good agreement, and the doublet structure in this valley is strikingly apparent in both curves. The small peak around III is noticeably shifted. There is no agreement for peak IV. Rieder originally speculated that peak IV may be due to a surface-proportional distribution of imperfections or perhaps to the presence of residual absorbed water molecules on the surface (although considerable effort was exerted to exclude water). However, our preliminary results on the influence of surface relaxation show that the big peak IV appears in the calculated $f^s(\omega)$ if we take a small inward surface relaxation into account.[32]

Finally, we should note two striking discrepancies remaining between our results for $f^s(\omega)$ and that derived in Refs. 3: (i) The flat-topped structure of peak I reported in Refs. 3 does not appear in our result. (ii) The scale of the $f^s(\omega)$ curve from Refs. 3, by use of the specific surface area of 110 m^2/g reported there, is about 4.4 times larger than the scale shown in Fig. 10; that is, the value of the maximum of peak II in Ref. 3(b) is 0.75 [when converted to $f^s(\omega)$ according to Eq. (35)], which is to be compared to the value of 0.21 for the peak II of the histogram. Although a simple histogram can underrepresent a peak height by as much as 50% when the channel width is about half the peak width, as in Fig. 10, the discrepancy in the peak amplitudes of the two curves for $f^s(\omega)$ is well outside such an allowance; when the staggered-bin smoothing of the histogram is considered, the discrepancy is even more definite. The experimental value of the specific surface area might be suspected. However, the 110-m^2/g value was determined from a fairly direct examination of particle size by means of electron micrographs and of x-ray line broadening, and that value is already 2.6 times larger than the surface area as determined by a BET (Brunauer-Emmett-Teller) adsorption analysis[3(b)]; to bring the experimental $f^s(\omega)$ curve into closer correspondence with the theoretical curve below 9×10^{13} rad/sec would require a further increase of the experimental surface area by at least another factor of 2. (As a point of comparison, our 15-layer MgO slab has a specific surface area of 177 m^2/g.) Clearly, additional work will be required to resolve these significant discrepancies.[44]

V. SUMMARY

In this paper we present a self-contained outline of the dynamics of a crystal slab with shell-model interaction, and report results of a comprehensive study of the vibrational surface modes for the unrelaxed (001) faces of six alkali-halide crystals (RbF, RbCl, NaF, NaCl, NaI, LiF) and MgO, all having the rocksalt structure. The seven crystals were chosen because of a variety of theoretical and experimental interests in their surface dynamics.

In our numerical calculation of the dynamical matrix elements a substantial improvement in the convergence of the Coulomb lattice sums is obtained by the use of the incomplete-gamma-function transformation for the case of intraplanar interactions ($l_3'=l_3$). For the benefit of other workers in the field we present a complete list of the dynamical matrix elements of the Coulomb interactions.

The seven crystals considered are of two types: The crystals of type A (RbF, RbCl, and NaI) have a large absolute gap separating the optical and acoustic bulk bands; the crystals of type B (NaF, NaCl, LiF, and MgO) do not exhibit such an absolute gap. The appearance of the surface-mode branches is strongly affected by the structure of the bulk subbands. In the present investigation of the surface vibration of the (001) face of rocksalt-structured slabs, eight pairs of surface-mode branches are found in type-A crystals. Two of these are macroscopic, namely, the Rayleigh modes (which are S_1, along $\overline{\Gamma}\overline{M}$, and which may be S_1 or S_7 along $\overline{\Gamma}\overline{X}$, depending on anisotropy) and the Fuchs-Kliewer modes; and six of these pairs are microscopic, namely, S_2,S_3,S_4,S_5,S_6, and the long-wave SH surface waves along $\overline{\Gamma}\overline{X}$ (which may be S_7 or S_1, depending on anistropy). In type-B crystals, at least six pairs of surface-mode branches are found; of these S_2 and S_6 are rather unpredictable owing to the strong overlap of the acoustic and optical bulk bands. Generally speaking, each of the six bulk subbands, to the extent that they are separately distinguishable, would give rise to at least one pair of surface modes.

We find that the frequencies of the pure microscopic surface modes obtained for a 15-layer slab have approached, to high precision, the values that are appropriate to an infinitely thick crystal. The effects of slab thickness on macroscopic Rayleigh and long-wave SH surface modes are small except in a small region around the origin of the SBZ.

In the comparison with limited experimental results, we find the general agreements to be good for the inelastic-atomic-scattering experiments on Ne-LiF,[7] and He-LiF.[6] Some of the discrepancies between our calculations and Rieder's inelastic-neutron-scattering experiment[3] may be diminished by incorporating a small surface relaxation into the calculations (see also Ref. 44).

All in all, the results of our unrelaxed 15-layer slab with realistic shell-model interactions are reasonably good. The seven sets of dispersion curves, and the surface-excess spectral density $f^s(\omega)$ and Table I should provide a rather complete picture of the vibrational surface modes of the unrelaxed (001) face of rocksalt-structured slabs. It is to be hoped that a substantial amount of this information might be of interest to experimentalists, and that it will help stimulate further experimental interest in this area.

ACKNOWLEDGMENTS

We gratefully acknowledge the assistance of D. Stott Parker in a wide variety of computational matters that improved the computations reported here. Correspondence with Dr. Karl-Heinz Rieder stimulated our initial investigation of the rubidium halides, because of their absolute gap between the acoustical and optical bulk bands, and we thank him for a number of helpful comments.

APPENDIX A: OUTLINE OF SHELL-MODEL FORMULATION FOR AN IONIC CRYSTAL SLAB

In the reformulation of the equations of motion (8) and (9) it is customary to separate the force constants (5)–(7) into parts representing the short-range and long-range Coulomb parts, respectively, i.e.,

$$\Phi^G_{\alpha\beta}(\vec{l}\kappa;\vec{l}'\kappa')\rightarrow\Phi^G_{\alpha\beta}(\vec{l}\kappa;\vec{l}'\kappa')+X_\kappa X_{\kappa'}\Phi^c_{\alpha\beta}(\vec{l}\kappa;\vec{l}'\kappa'),\tag{A1}$$

$$\Phi^F_{\alpha\beta}(\vec{l}\kappa;\vec{l}'\kappa')\rightarrow\Phi^F_{\alpha\beta}(\vec{l}\kappa;\vec{l}'\kappa')+X_\kappa Y_{\kappa'}\Phi^c_{\alpha\beta}(\vec{l}\kappa;\vec{l}'\kappa'),\tag{A2}$$

$$\Phi^S_{\alpha\beta}(\vec{l}\kappa;\vec{l}'\kappa')\rightarrow\Phi^S_{\alpha\beta}(\vec{l}\kappa;\vec{l}'\kappa')+Y_\kappa Y_{\kappa'}\Phi^c_{\alpha\beta}(\vec{l}\kappa;\vec{l}'\kappa').\tag{A3}$$

With the various Coulomb interactions explicitly displayed, henceforth $\Phi^G_{\alpha\beta}$, $\Phi^F_{\alpha\beta}$, and $\Phi^S_{\alpha\beta}$ shall stand for the force constants for the core-core, core-shell, and shell-shell short-range interactions, respectively. $\Phi^c_{\alpha\beta}$ is the force constant for Coulomb interactions between positive unit charges.

Since the crystal is invariant under a translation through a two-dimensional lattice vector in the slab, the force constants $\Phi_{\alpha\beta}(\vec{\mathrm{l}}\kappa;\vec{\mathrm{l}}'\kappa')$ depend only on the difference of $\bar{\mathrm{l}}'$ and $\bar{\mathrm{l}}$:

$$\Phi_{\alpha\beta}(\vec{\mathrm{l}}\kappa;\vec{\mathrm{l}}'\kappa')=\Phi_{\alpha\beta}(l_3\kappa;l_3'\kappa';\bar{\mathrm{l}}'-\bar{\mathrm{l}}). \tag{A4}$$

This two-dimensional translational invariance of the force constants implies that the normal-mode solutions of Eq. (8) and (9) have the form of two-dimensional Bloch functions. Eliminating $\vec{\mathrm{u}}^S(\vec{\mathrm{l}}\kappa)$ in favor of a new quantity $\vec{\mathrm{w}}(\vec{\mathrm{l}}\kappa)$, which is the displacement of the center of the shell with respect to the core, we may write

$$\begin{aligned}u^c_\alpha(\vec{\mathrm{l}}\kappa)&=(\bar{N}M_\kappa)^{-1/2}Q_0\xi^c_\alpha(l_3\kappa)\\&\quad\times\exp(i\{\bar{\mathrm{q}}\cdot[\bar{\mathrm{r}}_0(\bar{\mathrm{l}})+\vec{\mathrm{r}}_0(l_3\kappa)]-\omega t\})\ ,\end{aligned} \tag{A5}$$

$$\begin{aligned}w_\alpha(\vec{\mathrm{l}}\kappa)&=u^s_\alpha(\vec{\mathrm{l}}\kappa)-u^c_\alpha(\vec{\mathrm{l}}\kappa)\\&=(\bar{N}M_\kappa)^{-1/2}Q_0\eta_\alpha(l_3\kappa)\\&\quad\times\exp(i\{\bar{\mathrm{q}}\cdot[\bar{\mathrm{r}}_0(\bar{\mathrm{l}})+\vec{\mathrm{r}}_0(l_3\kappa)]-\omega t\})\ ,\end{aligned} \tag{A6}$$

where $\bar{N}$ is the number of lattice points in a plane in the period of two-dimensional periodic boundary conditions, M_κ the mass of an ion with index κ, Q_0 an amplitude factor, and $\xi^c_\alpha(l_3\kappa)$ and $\eta_\alpha(l_3\kappa)$ polarization vectors; $\bar{\mathrm{q}}$ is a two-dimensional wave vector in the xy plane and ω is the vibrational frequency.

Using the expressions (A1)–(A6) to rewrite the equations of motion (8) and (9), we obtain after some algebraic manipulations the following eigenvalue equations in terms of ξ^c_α and η_α:

$$\begin{aligned}\omega^2_p(\bar{\mathrm{q}})\xi^c_\alpha(l_3\kappa;\bar{\mathrm{q}}p)={}&\sum_{l_3'\kappa'\beta}[G_{\alpha\beta}(l_3\kappa;l_3'\kappa';\bar{\mathrm{q}})+F^*_{\beta\alpha}(l_3'\kappa';l_3\kappa;\bar{\mathrm{q}})+F_{\alpha\beta}(l_3\kappa;l_3'\kappa';\bar{\mathrm{q}})\\&+S_{\alpha\beta}(l_3\kappa;l_3'\kappa';\bar{\mathrm{q}})+(X_\kappa+Y_\kappa)(X_{\kappa'}+Y_{\kappa'})C_{\alpha\beta}(l_3\kappa;l_3'\kappa';\bar{\mathrm{q}})]\xi^c_\beta(l_3'\kappa';\bar{\mathrm{q}}p)\\&+\sum_{l_3'\kappa'\beta}[F_{\alpha\beta}(l_3\kappa;l_3'\kappa';\bar{\mathrm{q}})+S_{\alpha\beta}(l_3\kappa;l_3'\kappa';\bar{\mathrm{q}})+(X_\kappa+Y_\kappa)Y_{\kappa'}C_{\alpha\beta}(l_3\kappa;l_3'\kappa';\bar{\mathrm{q}})]\eta_\beta(l_3'\kappa';\bar{\mathrm{q}}p),\end{aligned} \tag{A7}$$

$$\begin{aligned}0={}&\sum_{l_3'\kappa'\beta}[F^*_{\beta\alpha}(l_3'\kappa';l_3\kappa;\bar{\mathrm{q}})+S_{\alpha\beta}(l_3\kappa;l_3'\kappa';\bar{\mathrm{q}})+Y_\kappa(X_{\kappa'}+Y_{\kappa'})C_{\alpha\beta}(l_3\kappa;l_3'\kappa';\bar{\mathrm{q}})]\xi^c_\beta(l_3'\kappa';\bar{\mathrm{q}}p)\\&+\sum_{l_3'\kappa'\beta}[S_{\alpha\beta}(l_3\kappa;l_3'\kappa';\bar{\mathrm{q}})+Y_\kappa Y_{\kappa'}C_{\alpha\beta}(l_3\kappa;l_3'\kappa';\bar{\mathrm{q}})]\eta_\beta(l_3'\kappa';\bar{\mathrm{q}}p)\ ,\end{aligned} \tag{A8}$$

where we have used the following definition for the elements of the dynamical matrix:

$$H_{\alpha\beta}(l_3\kappa;l_3'\kappa';\bar{\mathrm{q}})=(M_\kappa M_{\kappa'})^{-1/2}\sum_{\bar{\mathrm{l}}'}\Phi^H(l_3\kappa;l_3'\kappa';\bar{\mathrm{l}}'-\bar{\mathrm{l}})\exp\{i\bar{\mathrm{q}}\cdot[\bar{\mathrm{r}}_0(\bar{\mathrm{l}}'-\bar{\mathrm{l}})+\vec{\mathrm{r}}_0(l_3'\kappa')-\vec{\mathrm{r}}_0(l_3\kappa)]\}\ , \tag{A9}$$

where $H=G$, F, S, or C.

The equations can be further condensed, and at the same time given a direct physical interpretation, by introducing two new dynamical matrix contributions, $\overleftrightarrow{\mathrm{R}}$ and $\overleftrightarrow{\mathrm{T}}$:

$$\begin{aligned}R_{\alpha\beta}(l_3\kappa;l_3'\kappa';\bar{\mathrm{q}})={}&G_{\alpha\beta}(l_3\kappa;l_3'\kappa';\bar{\mathrm{q}})\\&+T_{\alpha\beta}(l_3\kappa;l_3'\kappa';\bar{\mathrm{q}})+F^*_{\beta\alpha}(l_3'\kappa';l_3\kappa;\bar{\mathrm{q}})\end{aligned} \tag{A10}$$

$$T_{\alpha\beta}(l_3\kappa;l_3'\kappa';\bar{\mathrm{q}})=F_{\alpha\beta}(l_3\kappa;l_3'\kappa';\bar{\mathrm{q}})+S_{\alpha\beta}(l_3\kappa;l_3'\kappa';\bar{\mathrm{q}})\ . \tag{A11}$$

Note that the same-site ($l_3\kappa=l_3'\kappa'$) shell-core coupling in $\overleftrightarrow{\mathrm{F}}$ and $\overleftrightarrow{\mathrm{F}}^*$ is in $\overleftrightarrow{\mathrm{R}}$ and $\overleftrightarrow{\mathrm{T}}$ canceled by parts of the self-interaction coupling in $\overleftrightarrow{\mathrm{G}}$ and $\overleftrightarrow{\mathrm{S}}$, so that the only remaining same-site shell-core coupling in the equations of motion is in the self-interaction part of $\overleftrightarrow{\mathrm{S}}$ in Eq. (A8). Consequently, $\overleftrightarrow{\mathrm{R}}$ can be interpreted as arising from the short-range coupling between pairs of ions, with each ion taken as a unit. Similarly, $\overleftrightarrow{\mathrm{T}}$ arises from the short-range coupling between the displacement of an ion as a complete unit and the *relative* shell displacement of another ion. Substitution of $\overleftrightarrow{\mathrm{R}}$ and $\overleftrightarrow{\mathrm{T}}$ in Eqs. (A7) and (A8) yields

$$\begin{aligned}\omega^2_p(\bar{\mathrm{q}})\xi^c_\alpha(l_3\kappa;\bar{\mathrm{q}}p)={}&\sum_{l_3'\kappa'\beta}\{[R_{\alpha\beta}(l_3\kappa;l_3'\kappa';\bar{\mathrm{q}})+Z_\kappa Z_{\kappa'}C_{\alpha\beta}(l_3\kappa;l_3'\kappa';\bar{\mathrm{q}})]\xi^c_\beta(l_3'\kappa';\bar{\mathrm{q}}p)\\&+[T_{\alpha\beta}(l_3\kappa;l_3'\kappa';\bar{\mathrm{q}})+Z_\kappa Y_{\kappa'}C_{\alpha\beta}(l_3\kappa;l_3'\kappa';\bar{\mathrm{q}})]\eta_\beta(l_3'\kappa';\bar{\mathrm{q}}p)\}\ ,\end{aligned} \tag{A12}$$

$$0=\sum_{l_3'\kappa'\beta}\{[T^{*}_{\beta\alpha}(l_3'\kappa';l_3\kappa;\bar{\mathrm{q}})+Y_\kappa Z_{\kappa'}C_{\alpha\beta}(l_3\kappa;l_3'\kappa';\bar{\mathrm{q}})]\xi^{c}_{\beta}(l_3'\kappa';\bar{\mathrm{q}}p)$$
$$+[S_{\alpha\beta}(l_3\kappa;l_3'\kappa';\bar{\mathrm{q}})+Y_\kappa Y_{\kappa'}C_{\alpha\beta}(l_3\kappa;l_3'\kappa';\bar{\mathrm{q}})]\eta_\beta(l_3'\kappa';\bar{\mathrm{q}}p)\}\ . \tag{A13}$$

Usually, the assumption is made that the short-range forces are entirely due to shell-shell interactions; this expresses the original view of the shell model that the short-range interaction is dominated by the overlap and the distortion of the outer electron clouds and that, in the model, these effects are caused by the relative motions of the shells. In this approximation $\overleftrightarrow{\mathrm{R}}=\overleftrightarrow{\mathrm{T}}=\overleftrightarrow{\mathrm{S}}$ (which implies $\overleftrightarrow{\mathrm{G}}=\overleftrightarrow{\mathrm{F}}=\overleftrightarrow{0}$, except that $\overleftrightarrow{\mathrm{F}}\neq\overleftrightarrow{0}$ for a shell on its own core). An additional term in Eq. (A13) results from the self-interaction term of $S_{\alpha\beta}(l_3\kappa;l_3'\kappa';\bar{\mathrm{q}})$ (see Appendix B); we relabel $S_{\alpha\beta}(l_3\kappa;l_3'\kappa';\bar{\mathrm{q}})$ as $\mathcal{S}_{\alpha\beta}(l_3\kappa;l_3'\kappa';\bar{\mathrm{q}})$, which is expressed as

$$\mathcal{S}_{\alpha\beta}(l_3\kappa;l_3'\kappa';\bar{\mathrm{q}})=S_{\alpha\beta}(l_3\kappa;l_3'\kappa';\bar{\mathrm{q}})$$
$$+(M_\kappa M_{\kappa'})^{-1/2}\delta_{l_3l_3'}\delta_{\kappa\kappa'}\delta_{\alpha\beta}K_\kappa\ ; \tag{A14}$$

i.e., $\mathcal{S}_{\alpha\beta}$ includes the interaction of the core and the shell of the same ion, while $S_{\alpha\beta}$ does not. With this notation incorporated, Eqs. (A12) and (A13) can be written in matrix notation as

$$\omega^2\overleftrightarrow{\xi}^c=(\overleftrightarrow{\mathrm{R}}+\overleftrightarrow{\mathrm{Z}}_d\overleftrightarrow{\mathrm{C}}\overleftrightarrow{\mathrm{Z}}_d)\overleftrightarrow{\xi}^c+(\overleftrightarrow{\mathrm{T}}+\overleftrightarrow{\mathrm{Z}}_d\overleftrightarrow{\mathrm{C}}\overleftrightarrow{\mathrm{Y}}_d)\overleftrightarrow{\eta}\ , \tag{A15}$$

$$0=(\overleftrightarrow{\mathrm{T}}^{*\dagger}+\overleftrightarrow{\mathrm{Y}}_d\overleftrightarrow{\mathrm{C}}\overleftrightarrow{\mathrm{Z}}_d)\overleftrightarrow{\xi}^c+(\overleftrightarrow{\mathcal{S}}+\overleftrightarrow{\mathrm{Y}}_d\overleftrightarrow{\mathrm{C}}\overleftrightarrow{\mathrm{Y}}_d)\overleftrightarrow{\eta}\ . \tag{A16}$$

Here $\overleftrightarrow{\mathrm{Z}}_d$ and $\overleftrightarrow{\mathrm{Y}}_d$ are the diagonal matrices for the ion and shell charges; $\overleftrightarrow{\xi}^c$ and $\overleftrightarrow{\eta}$ the column matrices for the eigenvectors of cores and shells, respectively; $\overleftrightarrow{\mathrm{R}}=\overleftrightarrow{\mathrm{T}}=\overleftrightarrow{\mathcal{S}}$ and $\overleftrightarrow{\mathrm{C}}$ the nondiagonal matrices for the interactions, in which the masses of the ions have been absorbed. Finally, Eqs. (A15) and (A16) can be combined and written in the form given in Eqs. (10) and (11).

APPENDIX B: SELF-INTERACTION ELEMENTS

The self-interaction elements of the shell-shell interaction matrix can be written as [cf. Eq. (A9)]

$$S_{\alpha\beta}(l_3\kappa;l_3\kappa;\bar{\mathrm{q}})=(1/M_\kappa)\Phi^{s}_{\alpha\beta}(l_3\kappa,l_3\kappa;0)+S'_{\alpha\beta}\ , \tag{B1}$$

where

$$S'_{\alpha\beta}=\frac{1}{M_\kappa}\sum_{\bar{\mathrm{l}}'}{}'\Phi^{s}_{\alpha\beta}(l_3\kappa;l_3\kappa;\bar{\mathrm{l}}'-\bar{\mathrm{l}})\exp[i\bar{\mathrm{q}}\cdot\bar{\mathrm{r}}(\bar{\Gamma}'-\bar{\Gamma})] \tag{B2}$$

The prime on the summation indicates that the term $\bar{\Gamma}'=\bar{\Gamma}$, which is the first term in the right hand side of Eq. (B1), has to be omitted. We further have

$$\Phi^{s}_{\alpha\beta}(l_3\kappa;l_3\kappa;0)=-\sum_{\bar{\mathrm{l}}'l_3'\kappa'}{}'\Phi^{s}_{\alpha\beta}(l_3\kappa;l_3'\kappa',\bar{\Gamma}'-\bar{\Gamma})$$
$$-\sum_{\bar{\mathrm{l}}'l_3'\kappa'}\Phi^{F}_{\beta\alpha}(l_3'\kappa';l_3\kappa,\bar{\Gamma}-\bar{\Gamma}')\ . \tag{B3}$$

the prime on the first summation indicates that the term $\bar{\mathrm{l}}'=\bar{\mathrm{l}}$, $l_3'=l_3$, $\kappa'=\kappa$ is to be omitted. Relation (B3) follows from the requirement that the forces on the shells remain zero if an arbitrary translation is performed on the lattice in its equilibrium configuration, i.e., from the condition $0=-F^{s}_{\alpha}(\vec{\mathrm{l}}\kappa)=\partial\Phi_2/\partial u^{s}_{\alpha}(\vec{\mathrm{l}}\kappa)$, where Φ_2 is given by Eq. (4).

The matrix elements $\Phi^{F}_{\alpha\beta}$ describe the core-shell interactions; in particular, $\Phi^{F}_{\alpha\beta}(l_3\kappa;l_3\kappa;0)$ describes the interaction between the core and the shell of the same ion. Since in the shell model this interaction is described by an isotropic spring of constant K_κ, we have

$$\Phi^{F}_{\alpha\beta}(l_3\kappa;l_3\kappa;0)=-K_\kappa\delta_{\alpha\beta}\ . \tag{B4}$$

Substituting Eq. (B4) in Eq. (B3) we have

$$\Phi^{S}_{\alpha\beta}(l_3\kappa;l_3\kappa;0)=-\sum_{\bar{\mathrm{l}}'l_3'\kappa'}{}'[\Phi^{S}_{\alpha\beta}(l_3\kappa;l_3'\kappa';\bar{\mathrm{l}}'-\bar{\mathrm{l}})$$
$$+\Phi^{F}_{\beta\alpha}(l_3'\kappa';l_3\kappa;\bar{\mathrm{l}}-\bar{\mathrm{l}}')]+K_\kappa\delta_{\alpha\beta}$$
$$=-\sum_{\bar{\mathrm{l}}'l_3'\kappa'}{}'\Phi^{T}_{\alpha\beta}(l_3\kappa;l_3'\kappa';\bar{\mathrm{l}}'-\bar{\mathrm{l}})+K_\kappa\delta_{\alpha\beta}, \tag{B5}$$

where we have used the relation

$$\Phi^{T}_{\alpha\beta}(l_3\kappa;l_3'\kappa';\bar{\mathrm{l}}'-\bar{\mathrm{l}})$$
$$=\Phi^{S}_{\alpha\beta}(l_3\kappa;l_3'\kappa';\bar{\mathrm{l}}'-\bar{\mathrm{l}})+\Phi^{F}_{\beta\alpha}(l_3'\kappa';l_3\kappa;\bar{\mathrm{l}}-\bar{\mathrm{l}}'),$$

which follows from Eq. (A11). It now follows from (B3) that

$$\Phi^{T}_{\alpha\beta}(l_3\kappa;l_3\kappa;0)=-\sum_{\bar{\mathrm{l}}'l_3'\kappa'}{}'\Phi^{T}_{\alpha\beta}(l_3\kappa;l_3'\kappa';\bar{\mathrm{l}}'-\bar{\mathrm{l}}); \tag{B6}$$

hence

$$\Phi^{S}_{\alpha\beta}(l_3\kappa;l_3\kappa;0)=\Phi^{T}_{\alpha\beta}(l_3\kappa;l_3\kappa;0)+K_\kappa\delta_{\alpha\beta}. \tag{B7}$$

Substitution of (B7) in (B1) gives

$$S_{\alpha\beta}(l_3\kappa;l_3\kappa;\bar{\mathrm{q}})=(1/M_\kappa)[\Phi^{T}_{\alpha\beta}(l_3\kappa;l_3\kappa;0)+K_\kappa\delta_{\alpha\beta}]+S'_{\alpha\beta}. \tag{B8}$$

The assumption that the short-range interaction between the ions is entirely due to the shell-shell interaction, leads to the following equalities:

$$\overleftrightarrow{G}=\overleftrightarrow{F}=0,\quad \overleftrightarrow{R}=\overleftrightarrow{T}=\overleftrightarrow{S}, \tag{B9}$$

while $\overleftrightarrow{F}\neq 0$ for the core-shell interaction on the same ion.

In Eq. (B8) we now rename the matrix element $S_{\alpha\beta}$ as $\mathcal{S}_{\alpha\beta}$ and replace $\Phi^T_{\alpha\beta}$ by $\Phi^S_{\alpha\beta}$ according to (B9); we then have

$$\begin{aligned}\mathcal{S}_{\alpha\beta}(l_3\kappa;l_3\kappa;\overline{q}) &= (1/M_\kappa)\Phi^s_{\alpha\beta}(l_3\kappa,l_3\kappa;0)\\ &\quad+S'_{\alpha\beta}+(1/M_\kappa)K_\kappa\delta_{\alpha\beta}\\ &=S_{\alpha\beta}(l_3\kappa;l_3\kappa;\overline{q})+(1/M_\kappa)K_\kappa\delta_{\alpha\beta}.\end{aligned} \tag{B10}$$

$\mathcal{S}_{\alpha\beta}(l_3\kappa;l_3\kappa;\overline{q})$ is the self-interaction element of the dynamical matrix of a shell model in which the ions have internal structure, i.e., an isotropic spring with constant K_κ connecting the core and the shell of the same ion. The element $S_{\alpha\beta}(l_3\kappa;l_3\kappa;\overline{q})$ is now defined as the self-interaction element of the dynamical matrix of a shell model without this internal structure.

For the case $l'_3\neq l_3$, $\kappa'=\kappa$ we have the following relation:

$$\begin{aligned}\mathcal{S}_{\alpha\beta}(l_3\kappa;l'_3\kappa';\overline{q}) &= S_{\alpha\beta}(l_3\kappa;l'_3\kappa';\overline{q})\\ &\quad+(M_\kappa M_{\kappa'})^{-1/2}\delta_{l_3l'_3}\delta_{\kappa\kappa'}\delta_{\alpha\beta}K_\kappa.\end{aligned} \tag{B11}$$

APPENDIX C: DYNAMICAL MATRIX ELEMENTS FOR A NaCl (001) SLAB

1. Short-range contributions

a. $\kappa\neq\kappa'$

$$R_{\alpha\beta}(l_3\kappa;l'_3\kappa';\overline{q})=0,\quad \text{if } \alpha\neq\beta \tag{C1}$$

(i) If $l_3+l'_3$ is even,

$$R_{xx}(l_3\kappa;l'_3\kappa';\overline{q})=\tfrac{1}{2}Q(A^{+-}c_x+B^{+-}c_y)\delta_{l_3,l'_3}, \tag{C2}$$

$$R_{yy}(l_3\kappa;l'_3\kappa';\overline{q})=\tfrac{1}{2}Q(B^{+-}c_x+A^{+-}c_y)\delta_{l_3,l'_3}, \tag{C3}$$

$$R_{zz}(l_3\kappa;l'_3\kappa';\overline{q})=\tfrac{1}{2}QB^{+-}(c_x+c_y)\delta_{l_3,l'_3}, \tag{C4}$$

where $Q=-e^2/r_0^3(M\kappa M\kappa')^{1/2}$, $c_\alpha=\cos(q_\alpha r_0)$ $(\alpha==x,y)$.

(ii) If $l_3+l'_3$ is odd,

$$R_{xx}(l_3\kappa;l'_3\kappa';\overline{q})=R_{yy}=\tfrac{1}{4}QB^{+-}(\delta_{l_3,l'_3+1}+\delta_{l_3,l'_3-1}), \tag{C5}$$

$$R_{zz}(l_3\kappa;l'_3\kappa';\overline{q})=\tfrac{1}{4}QA^{+-}(\delta_{l_3,l'_3+1}+\delta_{l_3,l'_3-1}). \tag{C6}$$

b. $\kappa=\kappa'$

(i) If $l_3+l'_3$ is even,

$$\begin{aligned}R_{xx}(l_3\kappa;l'_3\kappa;\overline{q})=R_{yy}=P[&\tfrac{1}{2}A^{+-}+B^{+-}+A^{\kappa\kappa}+2B^{\kappa\kappa}\\ &-\tfrac{1}{2}(A^{\kappa\kappa}+B^{\kappa\kappa})c_xc_y]\delta_{l_3,l'_3},\end{aligned} \tag{C7}$$

$$\begin{aligned}R_{zz}(l_3\kappa;l'_3\kappa;\overline{q})=P(&\tfrac{1}{2}A^{+-}+B^{+-}+A^{\kappa\kappa}+2B^{\kappa\kappa}\\ &-B^{\kappa\kappa}c_xc_y)\delta_{l_3,l'_3},\end{aligned} \tag{C8}$$

$$R_{xy}(l_3\kappa;l'_3\kappa;\overline{q})=\tfrac{1}{2}P(A^{\kappa\kappa}-B^{\kappa\kappa})s_xs_y\delta_{l_3,l'_3}, \tag{C9}$$

$$R_{xz}(l_3\kappa;l'_3\kappa;\overline{q})=R_{yz}(l_3\kappa;l'_3\kappa;\overline{q})=0. \tag{C10}$$

For a surface layer,

$$\begin{aligned}R^s_{xx}=R^s_{yy}=\tfrac{1}{4}P[&2A^{+-}+3B^{+-}+3A^{\kappa\kappa}\\ &+5B^{\kappa\kappa}-2(A^{\kappa\kappa}+B^{\kappa\kappa})c_xc_y]\delta_{l_3,l'_3},\end{aligned} \tag{C11}$$

$$R^s_{zz}=\tfrac{1}{4}P(A^{+-}+4B^{+-}+2A^{\kappa\kappa}+6B^{\kappa\kappa}-4B^{\kappa\kappa}c_xc_y)\delta_{l_3,l'_3}, \tag{C12}$$

where $P=e^2/r_0^3M_\kappa$, $s_\alpha=\sin(q_\alpha r_0)$, $(\alpha=x,y)$.

(ii) If $l_3+l'_3$ is odd,

$$\begin{aligned}R_{xx}(l_3\kappa;l'_3\kappa;\overline{q})=-\tfrac{1}{4}P[&(A^{\kappa\kappa}+B^{\kappa\kappa})c_x+2B^{\kappa\kappa}c_y]\\ &\times(\delta_{l_3,l'_3+1}+\delta_{l_3,l'_3-1}),\end{aligned} \tag{C13}$$

$$\begin{aligned}R_{yy}(l_3\kappa;l'_3\kappa;\overline{q})=-\tfrac{1}{4}P[&(A^{\kappa\kappa}+B^{\kappa\kappa})c_y+2B^{\kappa\kappa}c_x]\\ &\times(\delta_{l_3,l'_3+1}+\delta_{l_3,l'_3-1}),\end{aligned} \tag{C14}$$

$$\begin{aligned}R_{zz}(l_3\kappa;l'_3\kappa;\overline{q})=-\tfrac{1}{4}P(&A^{\kappa\kappa}+B^{\kappa\kappa})(c_x+c_y)\\ &\times(\delta_{l_3,l'_3+1}+\delta_{l_3,l'_3-1}),\end{aligned} \tag{C15}$$

$$R_{xy}(l_3\kappa;l'_3\kappa;\overline{q})=0, \tag{C16}$$

$$\begin{aligned}R_{xz}(l_3\kappa;l'_3\kappa;\overline{q})=-(i/4)P(&A^{\kappa\kappa}-B^{\kappa\kappa})\\ &\times s_x(-\delta_{l_3,l'_3+1}+\delta_{l_3,l'_3-1}),\end{aligned} \tag{C17}$$

$$\begin{aligned}R_{yz}(l_3\kappa;l'_3\kappa;\overline{q})=-(i/4)P(&A^{\kappa\kappa}-B^{\kappa\kappa})\\ &\times s_y(-\delta_{l_3,l'_3+1}+\delta_{l_3,l'_3-1}).\end{aligned} \tag{C18}$$

2. Coulomb contributions

a. $l''_3\equiv l_3-l'_3\neq 0$

$$C_{xx}(l_3\kappa;l'_3\kappa';\overline{q})=G\sum_{\mu_1\mu_2}Hf_A\frac{U^2}{T}\exp(-|l''_3|T), \tag{C19}$$

$$C_{yy}(l_3\kappa;l'_3\kappa';\overline{q})=G\sum_{\mu_1\mu_2}Hf_A\frac{V^2}{T}\exp(-|l''_3|T), \tag{C20}$$

$$C_{zz}(l_3\kappa;l'_3\kappa';\overline{q})=-(C_{xx}+C_{yy}), \tag{C21}$$

$$C_{xy}(l_3\kappa;l'_3\kappa';\overline{q})=G\sum_{\mu_1\mu_2}Hf_A\frac{UV}{T}\exp(-|l''_3|T), \tag{C22}$$

$$C_{xz}(l_3\kappa;\, l_3'\kappa';\, \bar{\mathrm{q}}) = iG \sum_{\mu_1\mu_2} H f_A U \frac{l_3''}{|l_3''|} \exp(-|l_3''|T)\,, \tag{C23}$$

$$C_{yz}(l_3\kappa;\, l_3'\kappa';\, \bar{\mathrm{q}}) = iG \sum_{\mu_1\mu_2} H f_A V \frac{l_3''}{|l_3''|} \exp(-|l_3''|T)\,, \tag{C24}$$

where $f_A = [1+(-1)^{\mu_1+\mu_2}]$, $U = \pi\mu_1 + q_x r_0$, $V = \pi\mu_2 + q_y r_0$, $T = (U^2+V^2)^{1/2}$; and (i) if $\kappa = \kappa'$, then

$$G = \pi/2r_0^3 M_\kappa, \quad H = \begin{cases} 1, & \text{if } l_3 + l_3' \text{ is even} \\ (-1)^{\mu_1}, & \text{if } l_3 + l_3' \text{ is odd;} \end{cases}$$

and (ii) if $\kappa \neq \kappa'$, then

$$G = \pi/2r_0^3 (M_\kappa M_{\kappa'})^{1/2}, \quad H = \begin{cases} (-1)^{\mu_1+1}, & \text{if } l_3 + l_3' \text{ is even} \\ -1, & \text{if } l_3 + l_3' \text{ is odd.} \end{cases}$$

b. $l_3'' \equiv l_3 - l_3' = 0$

$$\begin{aligned} C_{xx}(l_3\kappa;\, l_3\kappa';\, \bar{\mathrm{q}}) = {} & \frac{1}{M_\kappa}\Phi_{xx}(l_3\kappa;\, l_3'\kappa';\, \bar{\mathrm{q}}) + \frac{2W}{\pi^{1/2}} \sum_{\mu_1=1}^{\infty}\sum_{\mu_2=1}^{\infty} \frac{1}{N^{2/3}}[(s+f_B)\cos\theta + (s+f_c)\cos\phi]\left(\frac{M}{N}\Gamma(\tfrac{5}{2}, \alpha N) + \tfrac{1}{2}\Gamma(\tfrac{3}{2}, \alpha N)\right) \\ & + \frac{2W}{\pi^{1/2}} \sum_{\mu=1}^{\infty} (s+f_D)\frac{1}{\mu^3}[(c_{\mu x} - c_{\mu y})\Gamma(\tfrac{5}{2}, \alpha\mu^2) + \tfrac{1}{2}(c_{\mu x} + c_{\mu y})\Gamma(\tfrac{3}{2}, \alpha\mu^2)] \\ & - \frac{\pi^{1/2}}{4} W \sum_{\mu_1\mu_2} J f_A T\left[\frac{U^2 - V^2}{T^2}\Gamma\left(\tfrac{1}{2}, \frac{T^2}{4\alpha}\right) - \tfrac{1}{2}\Gamma\left(-\tfrac{1}{2}, \frac{T^2}{4\alpha}\right)\right] + \frac{2}{3\pi^{1/2}} W\alpha^{3/2}\delta_{\kappa,\kappa'}\,, \end{aligned} \tag{C25}$$

where $f_B = (-1)^{\mu_1+\mu_2+1}$, $f_C = (-1)^{\mu_1-\mu_2+1}$, $f_D = (-1)^{\mu_1+1}$, $\alpha = 1.75$, $N = \mu_1^2 + \mu_2^2$, $M = \mu_1^2 - \mu_2^2$, $\theta = \mu_1 q_x r_0 + \mu_2 q_y r_0$, $\phi = \mu_1 q_x r_0 - \mu_2 q_y r_0$, $C_{\mu\alpha} = \cos(\mu q_\alpha r_0)$, $(\alpha = x, y)$, $\Gamma(n, x) = \int_x^\infty e^{-t} t^{n-1} dt$;and (i) if $\kappa = \kappa'$, then $W = 1/r_0^3 M_\kappa$, $s = -1$, $J = -1$; and (ii) if $\kappa \neq \kappa'$, then $W = 1/r_0^3(M_\kappa M_{\kappa'})^{1/2}$, $S = 1$, $J = (-1)^{\mu_1}$, and

$$\begin{aligned} \frac{1}{M_\kappa}\Phi_{xx}(l_3\kappa;\, l_3'\kappa';\, 0) = {} & -\frac{4W}{\pi^{1/2}} \sum_{\mu_1=1}^{\infty}\sum_{\mu_2=1}^{\infty} \frac{1}{N^{3/2}}(f_B + f_C)\left(\frac{M}{N}\Gamma(\tfrac{5}{2}, \alpha N) + \tfrac{1}{2}\Gamma(\tfrac{3}{2}, \alpha N)\right) \\ & + \frac{\pi^{3/2}}{4} W \sum_{\mu_1\mu_2} [(-1) + (-1)^{\mu_1}] f_A N^{1/2}\left[\frac{M}{N}\Gamma\left(\tfrac{1}{2}, \frac{N}{4\alpha}\right) - \tfrac{1}{2}\Gamma\left(-\tfrac{1}{2}, \frac{N}{4\alpha}\right)\right] \\ & - \frac{4W}{\pi^{1/2}} \sum_{\mu=1}^{\infty} \frac{1}{\mu^3} f_D \Gamma(\tfrac{3}{2}, \alpha\mu^2) - \frac{2}{3\pi^{1/2}} W\alpha^{3/2} \\ & - \frac{\pi^2}{2} W \sum_{\mu_1\mu_2}\left(\sum_{l_3''\neq 0}^{\text{even}} - \sum_{l_3''\neq 0}^{\text{odd}}\right)[1 + (-1)^{\mu_1+1}] f_A \frac{\mu_1^2}{N^{1/2}} \exp(-|l_3''|N^{1/2})\,. \end{aligned}$$

$C_{yy}(l_3\kappa;\, l_3\kappa';\, \bar{\mathrm{q}})$ can be obtained by exchanging q_x and q_y in C_{xx}.

$$C_{xy}(l_3\kappa;\, l_3\kappa';\, \bar{\mathrm{q}}) = \frac{4W}{\pi^{1/2}} \sum_{\mu_1=1}^{\infty}\sum_{\mu_2=1}^{\infty} \frac{\mu_1\mu_2}{N^{5/2}}[(s+f_B)\cos\theta - (s+f_C)\cos\phi]\Gamma(\tfrac{5}{2}, \alpha N) - \frac{\pi^{1/2}}{2} W \sum_{\mu_1\mu_2} J f_A \frac{UV}{T}\Gamma\left(\tfrac{1}{2}, \frac{T^2}{4\alpha}\right), \tag{C26}$$

$$C_{xz}(l_3\kappa;\, l_3\kappa';\, \bar{\mathrm{q}}) = C_{yz}(l_3\kappa;\, l_3\kappa';\, \bar{\mathrm{q}}) = 0\,. \tag{C27}$$

---

*Research supported in part by the Robert A. Welch Foundation, by AFOSR Grant No. 71-1973 and NSF Grant No. DMR 75-18492.

†Much of work by G.P.A. reported here was carried out at the University of Texas at Austin; work at the University of Missouri-Rolla supported in part by AFOSR Grant No. 76-2938.

[1] H. Boersch, J. Geiger, and W. Stickel, Phys. Rev. Lett. 17, 379 (1966); Z. Phys. 212, 130 (1968).

[2] H. Ibach, Phys. Rev. Lett. 24, 1416 (1970).

[3] (a) K. H. Rieder and E. M. Hörl, Phys. Rev. Lett. 20, 209 (1968); (b) K. H. Rieder, Surf. Sci. 26, 637 (1971).

[4] K. H. Rieder and W. Drexel, Phys. Rev. Lett. 34, 148 (1975).

[5] T. P. Martin, Phys. Rev. 177, 1349 (1969); Phys. Rev. B 1, 3480 (1970); L. Genzel and T. P. Martin, Phys. Status Solidi B 51, 91 (1972).

[6] (a) B. R. Williams, J. Chem. Phys. 55, 3220 (1971); 56, 1895 (1972); (b) B. F. Mason and B. R. Williams, J. Chem. Phys. 61, 2765 (1974).

[7] G. Benedek, Phys. Rev. Lett. 35, 234 (1975), and references therein.

[8] R. Fuchs and K. L. Kliewer, Phys. Rev. 140, A2076 (1965); K. L. Kliewer and R. Fuchs, Phys. Rev. 144, 495 (1966); 150, 573 (1966).

[9] R. Englman and R. Ruppin, Phys. Rev. Lett. 16, 898 (1966); R. Ruppin and R. Englman, Rep. Prog. Phys. 33, 149 (1970).

[10] A. A. Lucas, J. Chem. Phys. 48, 3156 (1968).

[11] S. Y. Tong and A. A. Maradudin, Phys. Rev. 181, 1318 (1969).

[12] T. S. Chen, R. E. Allen, G. P. Alldredge, and F. W. de Wette, Solid State Commun. 8, 2105 (1970).

[13] W. E. Jones and R. Fuchs, Phys. Rev. B 4, 3581 (1971).

[14] T. S. Chen. G. P. Alldredge, F. W. de Wette, and R. E. Allen, Phys. Rev. B 6, 627 (1972).

[15] T. S. Chen, Ph. D. dissertation (The University of Texas at Austin, 1971) (unpublished), available as order No. 72-15726, University Microfilms, Ann Arbor, Mich. 48106.

[16] T. S. Chen, G. P. Alldredge, F. W. de Wette, and R. E. Allen, Phys. Rev. Lett. 26, 1543 (1971).

[17] T. S. Chen, G. P. Alldredge, and F. W. de Wette, Solid State Commun. 10, 941 (1972).

[18] (a) T. S. Chen, G. P. Alldredge, and F. W. de Wette, Phys. Lett. 40A, 401 (1972); (b) 46A, 91 (1973).

[19] P. D. Schulze, Phys. Rev. B 14, 794 (1976).

[20] L. Genzel and T. P. Martin, Phys. Status Solidi B 51, 101 (1972).

[21] G. Benedek, Phys. Status Solidi B 58, 661 (1973).

[22] E. W. Kellermann, Philos. Trans. R. Soc. Lond. A 238, 513 (1940).

[23] B. G. Dick, Jr. and A. W. Overhauser, Phys. Rev. 112, 90 (1958).

[24] A. D. B. Woods, W. Cochran, and B. N. Brockhouse, Phys. Rev. 119, 980 (1960).

[25] W. Cochran, Adv. Phys. 10, 401 (1961).

[26] R. A. Cowley, Proc. R. Soc. A 268, 109 (1962); 268, 121 (1962).

[27] M. J. P. Musgrave, *Crystal Acoustics* (Holden-Day, San Francisco, 1970).

[28] S. K. Sinha, Crit. Rev. Solid State Sci. 3, 273 (1973).

[29] G. Venkataraman, L. A. Feldkamp, and V. C. Sahni, *Dynamics of Perfect Crystals* (MIT, Cambridge, Mass., 1975).

[30] R. E. Allen, G. P. Alldredge, and F. W. de Wette, Phys. Rev. B 4, 1648 (1971).

[31] G. C. Benson and T. A. Claxton, J. Chem. Phys. 48, 1356 (1968).

[32] T. S. Chen, G. P. Alldredge, and F. W. de Wette, Bull. Am. Phys. Soc. 20, 490 (1975).

[33] F. W. de Wette and G. E. Schacher, Phys. Rev. 137, A78 (1965); 138, erratum AB4 (1965).

[34] (a) LiF: G. Dolling, H. G. Smith, R. M. Nicklow, P. R. Vijayaraghavan, and M. K. Wilkinson, Phys. Rev. 168, 970 (1968), model I; (b) MgO: M. J. L. Sangster, G. Peckham, and D. H. Saunderson, J. Phys. C 3, 1026 (1970), model B; (c) NaF: W. J. L. Buyers, Phys. Rev. 153, 923 (1967), model VI; (d) NaCl: R. G. Schmunk and D. R. Winder, J. Phys. Chem. Solids 31, 131 (1970); (e) NaI: R. A. Cowley, W. Cochran, B. N. Brockhouse, and A. D. B. Woods, Phys. Rev. 131, 1030 (1963), model VI; (f) RbF and RbCl: G. Raunio and S. Rolandson, Phys. Rev. B 2, 2098 (1970); 6, E2511 (1972).

[35] F. W. de Wette and G. P. Alldredge, in *Methods of Computational Physics*, edited by G. Gilat, B. Alder, S. Fernbach, and M. Rotenberg (Academic, New York, 1975), Vol. 15, p. 163.

[36] T. S. Chen, G. P. Alldredge, and F. W. de Wette, Surf. Sci. 56, 25 (1976).

[37] G. P. Alldredge, Phys. Lett. 41A, 281 (1972); V. L. Zoth, G. P. Alldredge, and F. W. de Wette, Phys. Lett. 47A, 247 (1974).

[38] See, for example, the review by G. W. Farnell, in *Physical Acoustics*, edited by W. P. Mason and R. N. Thurston (Academic, New York, 1970), Vol. 6, p. 109. We reserve the term "Rayleigh mode" for the wave described by Rayleigh and its generalizations which are derivable from elastic continuum theory and which have elliptical particle motion confined primarily to the sagittal plane.

[39] K. L. Kliewer and R. Fuchs, Adv. Chem. Phys. 27, 355 (1974).

[40] T. C. Lim and G. W. Farnell, J. Appl. Phys. 39, 4319 (1968); F. R. Rollins, T. C. Lim, and G. W. Farnell, Appl. Phys. Lett. 12, 236 (1968).

[41] The experimental values and GF theoretical values for R_M and L_P have been supplied by G. Benedek (private communication and unpublished).

[42] Very recently, both G. Boato and G. Benedek have informed us that recent experiments at Genoa have revealed that the prominent inelastic features, interpreted in Ref. 7 as critical-point surface-phonon features, have major contributions arising from inelastic processes involving bound states of the atom-surface potential. Given the experimental resolution presently available, the bound-state resonance effects may completely overshadow the surface-phonon singularity effects predicted in Ref. 7, so that more refined work will be required before the analysis of inelastic atom scattering from surfaces can be expected to give solid evidence for surface-phonon bands.

[43] W. Weber, Phys. Rev. B 8, 5082 (1973).

[44] In response to an early draft of this paper, Rieder (private communication) has suggested an interesting hypothesis for the origin of the major discrepancy between theoretical and experimental amplitudes of $f^s(\omega)$ for MgO. The large slow-neutron cross section of hydrogen (about 20 times greater than either Mg or O) means that a relatively low *surface* concentration of hydroxl ions, say replacing a few percent of the surface oxygen ions, would enhance significantly the contributions of the surface particles to the inelastic neutron scattering. The effect would be to make the sample appear to have more surface particles than there actually are present. This hypothesis is a significant one and will require further examination. There are, of course, some obvious complications, bearing primarily on the kinds of defect modes set up by hydroxl ions substituting for oxygen ions on the surface. The O-H stretch frequency is far above the upper limit of the MgO phonon density of states and the mass change is rather small, but the coupling constant, ion charge, and static dipole changes are very significant and could to lead to some apparent distortion of the experimentally inferred $f^s(\omega)$.